

# 2013 March 17 Storm: Synergy of Observations Related to Electric Field Modes and their Ionospheric and Magnetospheric Effects

*L. R. Lyons<sup>1</sup>, B. Gallardo-Lacourt<sup>1</sup>, S. Zou<sup>2</sup>, J. M. Weygand<sup>3</sup>, Y. Nishimura<sup>1</sup>, W. Li<sup>1</sup>, M Gkioulidou<sup>4</sup>, V. Angelopoulos<sup>3</sup>, E. F. Donovan<sup>5</sup>, J. M. Ruohoniemi<sup>6</sup>, B. J. Anderson<sup>7</sup>, S. G. Shepherd<sup>8</sup>, N. Nishitani<sup>9</sup>*

<sup>1</sup>Department of Atmospheric and Oceanic Sciences, University of California, Los Angeles, CA 90095-1555 USA ([larry@atmos.ucla.edu](mailto:larry@atmos.ucla.edu))

<sup>2</sup>Climate and Space Sciences and Engineering Department, University of Michigan, 2455 Hayward Street, Ann Arbor, MI 48109-2143

<sup>3</sup>Department of Earth, Planetary, and Space Sciences, University of California, Los Angeles, CA 90095-1567 USA.

<sup>4</sup>Applied Physics Laboratory, Johns Hopkins University, Laurel, Maryland, USA

<sup>5</sup>Department of Physics and Astronomy, University of Calgary, 2500 University Drive, Calgary, Alberta, Canada T2N 1N4

<sup>6</sup>Bradley Department of Electrical and Computer Engineering, Virginia Tech, Blacksburg, VA 24061, USA

<sup>7</sup>The Johns Hopkins University Applied Physics Laboratory, Laurel, MD, 20723, USA.

<sup>8</sup>Thayer School of Engineering, Dartmouth College, Hanover NH 03755

<sup>9</sup>Solar-Terrestrial Environment Laboratory, Nagoya University, Nagoya, Aichi 464-8601, Japan

Submitted to

This is the author manuscript accepted for publication and has undergone full peer review but has not been through the copyediting, typesetting, pagination and proofreading process, which may lead to differences between this version and the [Version of Record](#). Please cite this article as doi: [10.1002/2016JA023237](https://doi.org/10.1002/2016JA023237)

Journal of Geophysical Research

Revised October 2016

Author Manuscript

## Abstract

The main phase of the 2013 March 17 storm had excellent coverage from ground-based instruments and from low- and high-altitude spacecraft, allowing for evaluation of the relations between major storm-time phenomena that are often considered separately. The shock impact with its concurrent southward IMF immediately drove dramatic poleward expansion of the poleward boundary of the auroral oval (implying strong nightside reconnection), strong auroral activity, and strong penetrating mid-latitude convection and ionospheric currents. This was followed by periods of southward IMF driving of electric fields that were at first relatively smooth as often employed in storm modeling, but then became extremely bursty and structured associated with equatorward extending auroral streamers. The auroral oval did not expand much further poleward during these two latter periods, suggesting a lower overall nightside reconnection rate than that during the first period and approximate balance with dayside reconnection. Characteristics of these three modes of driving were reflected in horizontal and field-aligned currents. Equatorward expansion of the auroral oval occurred predominantly during the structured convection mode, when electric fields became extremely bursty. The period of this third mode also approximately corresponded to the time of largest equatorward motion of the ionospheric trough, of apparent transport of high TEC features into the auroral oval from the polar cap, and of largest earthward injection of ions and electrons into the ring current. The enhanced responses of the aurora, currents, TEC, and the ring current indicate a common driving of all these storm-time features during the bursty convection mode period.

## 1. Introduction

An essential feature of magnetic storms is the spatial extension of the disturbance convection, ionospheric currents, and particle precipitation to mid- and low-latitudes during the main phase. The features of interest here are the earthward penetration of the plasma sheet in the magnetotail (equatorward in the ionosphere), the equatorward expansion of the auroral oval, of oval-related ionospheric currents, and of the Region 2 (R2) field-aligned current (FAC) system, the equatorward motion of the poleward edge of mid-latitude ionospheric trough, the injection of particles to form the storm time ring current, and ionospheric density enhancements that move throughout the nightside auroral oval. Generally, these signatures are treated separately even though they share underlying physical processes. However, the richness of the extensive array of overlapping data sets for the 2013 March 17 storm gives us the opportunity to identify relationships between these disparate features and place their development in the context of a common dynamical origin.

The 2013 March 17 storm is a Coronal Mass Ejection (CME) driven event with a shock that impacted the magnetosphere at 06 UT [Baker *et al.*, 2014], and there has been much interest in ring current particle injections [e.g., Gkioulidou *et al.* [2014] and radiation belt electrons [e.g., Hudson *et al.*, 2015; Li *et al.*, 2014, 2015] for this event (the storm time radiation belt electron enhancement occurred after the period of interest here). During the main phase of this storm, we have excellent and overlapping coverage of the aurora from the array of THEMIS ground-based all-sky imagers (ASIs) [Mende *et al.*, 2008], of ionospheric flows from the ground-based Super Dual Auroral Radar Network (Super DARN) and the Poker Flat Incoherent Scatter radar (PFISR), of the global distribution of magnetic field-aligned currents (FACs) from the Active Magnetosphere and Planetary Electrodynamics Response Experiment

(AMPERE, <http://ampere.jhuapl.edu/index.html>) [Anderson et al., 2014], and of in-situ plasma sheet particles from the two Van Allen Probes (VAP A and B) [Mauk et al., 2013] and the THEMIS probes near the equatorial plane [Angelopoulos, 2008]. In addition to these, we also have the routinely available maps of vertical total electron content (TEC) from the Madrigal database [Rideout and Coster, 2006], magnetic fields from ground-based magnetometers, and particle measurements from the low-altitude, polar-orbiting, Defense Meteorological Satellite Program (DMSP) spacecraft. Here, we use these data to explore the possible common driving by mid-latitude electric fields of the penetration of the plasma sheet, auroral oval and its ionospheric currents, and of the R2 currents, major ionospheric density features, and the formation of the stormtime ring current. We find the existence of different modes of mid-latitude electric fields and currents during the main phase of this storm, and present evidence for which of the three modes is the most important for the driving of the above stormtime phenomena.

## 2. Radar and ASI Observations

Figure 1 shows, from top to bottom, the WIND solar wind dynamic pressure  $P_{dyn}$ , the OMNI interplanetary magnetic field (IMF) as propagated to the dayside magnetopause, the SuperMAG [Gjerloev, 2012] ground magnetometer upper U and lower L auroral magnetic index, the SuperMAG ring current index for all MLT and within the dusk, noon, dawn, and midnight sectors, and ground magnetometer observations from North American stations near 66-67° MLAT with increasing UT of midnight (indicated by small vertical arrows). These SuperMAG indices are based on the traditional AU, AL, and SYMH indices, but with many more, and well-distributed stations. The OMNI IMF data is shown further shifted by ~10 minutes so that the shock impact time agrees with the 0600 UT impact time seen by the dayside ground

magnetometers. The WIND  $P_{dyN}$  is shown because of data gaps in the OMNI  $P_{dyN}$  around the time of the shock. It is further shifted by  $\sim 30$  min relative to the IMF data to agree with the time of shock impact, and shows the large increase in  $P_{dyN}$  of the shock that impacted the magnetosphere. Maroon-colored dashed boxes identify the four main periods (periods 1-4) of southward IMF that were seen after the shock arrival and during the storm main phase, each being reflected in the auroral L index.

During the main phase period shown, the ring current index for all MLT decreased to  $-110$  nT, making this a moderate intensity storm. The individual magnetometer stations in Figure 1 show numerous fluctuations of the N (northward) component, however, only one decrease was associated with a substorm that could be identified in the auroral observations. Some decreases were clearly associated with the major southward turnings of the IMF, while most of the others do not correlate well between stations and were most likely associated with the longitudinally localized auroral streamers and flow bursts that are discussed later and seen in subsequent figures. Because of the localized nature of flow bursts, and the inclusion of substantially more magnetometer stations, the auroral L index is relatively smooth.

### *2.1 Post-shock southward IMF period 1 (0600-0616 UT)*

Movie S1 shows auroral images overlaid with line-of-sight (LOS) flow velocities from the SuperDARN radars from 0540-1300 UT, which includes the shock impact and the storm main phase development. Panels are shown every 30 s and include mergers of the images from all available ASIs over Canada and Alaska, and, from west to east, LOS flow velocities from the mid-latitude Christmas Valley west and east (CVW and CVE) and the Fort Hays west and east (FHW and FHE) radars (data taken with 60 s resolution). Occasional echoes are also seen in the

polar cap region, which are from the radar at Rankin Inlet. Representative snapshots from the movie are shown in Figure 2.

As seen in S1 and the first two panels of Figure 2, a narrow band of moderately active aurora lay along the poleward boundary of the evening-to-midnight auroral oval prior to the shock impact. This activity, and the lower than average location of the auroral poleward boundary (magnetic latitude  $\Lambda \sim 68^\circ - 70^\circ$ ), likely resulted from the pre-storm southward IMF of a few nT. The flows seen by the Super DARN radars show weak, and relatively uniform, east-to-west flow at sub-auroral mid-latitudes ( $\Lambda \sim 52^\circ$  to  $62^\circ$ ) as indicated by the observed flows being towards the radars in the eastward looking and away from the radars in the westward looking beams.

The dramatic effects of the shock impact can be seen in S1 and the next two panels (0602 and 0606 UT) of Figure 2. This includes a rapid, large poleward expansion of the auroral oval over a broad MLT range, which is a well-studied response to dynamic pressure impacts under prior southward IMF conditions [Boudouridis *et al.*, 2003; Zesta *et al.*, 2000]. There is also a very large increase in the mid-latitude, sub-auroral westward electric fields. These penetrating electric fields are part of the well-known global response to solar-wind dynamic pressure impacts [e.g., Hori *et al.*, 2012; Kikuchi *et al.*, 2001; Takahashi *et al.*, 2015; Zesta *et al.*, 2000].

The change in the auroral oval precipitation can be seen very clearly in the precipitation observations shown in Figure 3 from DMSP F17 and F16, which, respectively, traversed the southern hemisphere auroral oval and polar cap several minutes before and several minutes after the shock impact. For each spacecraft, integrated precipitating electron energy flux is shown in the top panel and energy-time spectrograms of precipitating electron and ion energy fluxes are

shown in the lower two panels. The auroral arc along the auroral boundary before the shock can clearly be seen as inverted-V structures in the F17 data on both the pre- and post-midnight crossings of the oval, and an  $\sim 2.5^\circ$  wide band of diffuse auroral precipitation can be seen at  $\sim 1$ - $10$  keV on the post-midnight crossing. This region of diffuse electron precipitation continues to be seen, with a small  $\sim 1^\circ$  equatorward displacement, on the post-shock F16 crossing  $\sim 18$  min later, the energy and fluxes of the precipitating electrons having been increased by the shock compression of the magnetosphere.

However, in addition, the post-shock crossing shows a broad region of strong structured electron precipitation, with peak energies within inverted-V regions extending to  $>10$  keV. This region extends poleward to  $\Lambda = 72.5^\circ$  and includes strong precipitation of  $\sim 10$  to  $>30$  keV protons, indicating that, within the  $\sim 10$  min period following the shock, a broad, active region of new plasma sheet with high proton energies had formed within a  $\sim 4^\circ$  wide region of previously open lobe field lines. A similar feature is seen on the pre-midnight crossing, but over a substantially narrower  $\sim 1.7^\circ$  wide latitude range. This new particle population, associated with the previously known rapid nightside reconnection across the nightside plasma sheet boundary that is driven by solar wind dynamic pressure impacts [Boudouridis *et al.*, 2004, 2005], gives a reservoir of energetic plasma that could be convected Earthward in the plasma sheet to become a feature of the storm time disturbance phenomena at lower latitudes.

## 2.2 Second southward IMF period (0635-0718 UT)

Figure 4 shows overviews of the ASI and radar data from 0500-1430 UT. The top 2 panels give keograms along a magnetic meridian somewhat to the west/east of the central meridian of the Fort Smith (FSMI)/Pinawa (PINA) ASI (the imager fields-of-view being shown in Figure 1). The FSMI keogram shows that the rapid poleward expansion and small



equatorward expansion of the oval after the shock impact during period 1 was followed by equatorward expansion of the oval to  $\Lambda \sim 66^\circ$  during period 2, the second period of southward IMF. An auroral enhancement at  $\Lambda \sim 66^\circ$  can also be seen to the east in the PINA keogram, where intensities rise to just above background at the end of this time period. The narrow, bright features in the FSMI keogram that extend across several degrees of latitude prior to southward IMF period 2 are keogram signatures of intense auroral streamers. However, such signatures of strong streamers are absent during period 2, and the equatorward expansion appears to be related to that of the diffuse auroral electron precipitation. This different behavior of the aurora between periods 1 and 2 is also apparent in movie S1.

The lower four panels of Figure 4 show LOS velocities of the mid-latitude radars that are averaged over 2 or 3 beams along the four directions that are drawn in the insert in the top right portion of the Figure. The first and third of these panels are from CVW and FHW beams looking northwestward toward the Gulf of Alaska and towards western Canada, respectively. The second is from CVW beams looking approximately poleward toward FSMI, and the fourth panel is from FHE beams looking northeastward over eastern Canada. The large blue dots give the equatorward boundary of plasma sheet electron precipitation as observed on the multiple crossings of the southern hemisphere auroral by the DMSP F16-F18 spacecraft, the MLT of observation given in blue above each dot. Pre-midnight crossings are shown in the poleward looking CVW panel, though these radar beams are only at pre-midnight MLTs until  $\sim 09$  UT, and post-midnight crossings are shown in the panel for the eastward looking FHE beams, which measure post-midnight after  $\sim 06$  UT. The modest equatorward expansion of the auroral oval is seen following period 2 in the electron precipitation boundaries between periods 2 and 3. That the precipitation boundaries are a few degrees equatorward of the detectable auroral boundary on the

pre-midnight side, is likely a result of the ASI detection threshold. As expected from particle drifts, the electron precipitation boundary is seen a few degrees further equatorward on the post-midnight side, where the DMSP crossings are downward of the PINA field-of-view at times prior to period 3.

As seen by the CVW and FHE radar beams in Figure 4 and the 0620 and 0701 UT panels of Figure 2, after decreasing substantially during the northward IMF in between periods 1 and 2, there was a very large increase in the mid-latitude, sub-auroral westward flows during period 2. While the flow speeds were similar to those seen during period 1, there was a distinct difference in the structuring of the convection. During the first period, the LOS plots in Figure 4 looked striped as a result of substantial flow variations that can be seen within the 60 s period from one radar scan to the next. These strong variations can be seen over many more radar beams in movie S1. On the other hand, the flow had far less structuring during period 2. It is interesting that a similar difference between the two periods is seen in the auroral observations at much higher latitudes, there being several short-lived bright features on the FSMI keogram during period 1 but only much more smoothly varying aurora during period 2. Consistent with the rapidly varying auroral activity seen during period 1, the DMSP F16 electron precipitation observations in Figure 3 show a large number of close-together, strong electron precipitation features.

### *2.3 Third southward IMF period (0757-1034 UT)*

During the first 1 ¼ hr of southward IMF period 3, the equatorward boundary of the aurora moved several degrees equatorward, from  $\Lambda \sim 66^\circ$  to  $\Lambda \sim 60^\circ$  in the PINA keogram. Furthermore, much more streamer activity occurred during period 3 than during period 2, as can be seen in S1 and the FSMI keogram. Also, a couple of omega bands become apparent at  $\Lambda <$

$\sim 64^\circ$  in the auroral observations from PINA, omega bands being a common feature on the morning side during periods of enhanced convection. The streamers continued throughout period 3, though they were not as intense and close together as during the post-shock period 1. Due to light contamination at lower latitudes, the streamers are seen only to  $\Lambda \sim 67^\circ$  by the FSMI keogram, but a few streamers can be discerned in S1 that extended to  $\Lambda \sim 62^\circ$ .

Very different mid-latitude convection features were seen during period 3 as compared to what was seen during period 2. As can be seen for all the beams in Figure 4, the convection became very bursty with LOS flow speeds varying from  $\sim 500$  m/s to close to 0 m/s repetitively over  $\sim 10$ -20 min periods. These bursts of enhanced flow have a strong equatorward component as shown by the poleward looking CVW beams (17,19,20), and the strong bursty behavior of the flows continues into the region of post-midnight eastward flows seen in the FHW and FHE panels. While these radar echoes are at the same mid-latitudes as during periods 1 and 2, the regions of echoes appear to move equatorward with the equatorward boundary of the aurora, particularly in the poleward looking CVW panel. This suggests that these mid-latitude echoes are within the expanding aurora oval, consistent with the equatorward boundaries of electron precipitation seen by the DMSP spacecraft.

As indicated by the pink and white arrows in the bottom panels of Figure 2, each individual flow burst during period 3 had a longitudinal width  $\lesssim 1$  hr in MLT, some being  $\ll 1$  hr in MLT. Additionally, based on the LOS flow speeds, many individual bursts did not extend across the full latitudinal extent of the radar echo region. While we are unable to track the two-dimensional evolution of individual flow bursts as function of time with only the LOS flows and 1 min time resolution, the existence of eastward going bursts on the dawnside of the echo region suggests that many flow bursts on the morning side turn azimuthally towards the east. We do not

have sufficient echoes during period 3 to determine if evening side bursts turn towards the west as has previously been seen [Kauristie et al., 2003; Zou et al., 2009]. However, there is evidence for a westward excursion of flow bursts near midnight, as indicated by the short white lines in the 0919 and 0920 UT panels of Figure 2.

Additionally, there are some radar echoes during period 3 that appear to be sub-auroral and show bursty flows, as identified in Figure 4. These have an equatorward component as seen by the poleward looking CVW beams, and a westward component in the eastward looking FHE beams. These flows are almost certainly within the sub-auroral polarization streams (SAPS) region, since the flows lay equatorward of the equatorward DSMP electron precipitation boundaries. The fact that these flows are bursty is consistent with some of the flow bursts within the auroral oval extending equatorward into the SAPS region and turning towards the west. We thus see evidence for a general guiding of the flow bursts by the large-scale convection pattern, flow bursts within the duskside convection being azimuthally turned to the west (some within the SAPS region) and those within the dawn cell being turned toward the east, consistent with recent implications from observations [Lyons et al., 2015].

## 2.2 Fourth southward IMF period (1100-1213 UT)

The bursty flow pattern continued during southward IMF period 4, the pattern being very similar to that during period 4. Enhanced bursts of flow can be seen in the equatorward and eastward flows, as well as in the westward sub-auroral flows. However, based on the DMSP equatorward electron boundaries in Figure 4 and the Alaskan ASI images in movie S1, the equatorward boundary of the auroral precipitation did not expand discernibly further equatorward during this period.

## 3. Equivalent ionospheric and field-aligned current systems.

The radar observations have indicated the existence of three different modes of mid-latitude electric field enhancements following the storm shock and during the storm main phase. In this section, we show how the post-shock, smoothly enhanced, and bursty enhanced convection modes are reflected in ionospheric and field-aligned current systems. Figure 5 shows ionospheric equivalent currents over North America obtained from ground based magnetometers (locations given by yellow stars) using the spherical elementary currents systems (SECS) approach [Amm and Viljanen, 1997; Weygand et al., 2011]. The top panel reproduces the poleward looking CVW panel from Figure 4, the four southward IMF periods being identified by maroon dashed lines and vertical magenta lines identifying the times of the SECS panels in the lower two rows.

The first equivalent current panel shows the pre-shock eastward current of the duskside DP2 cell lying at  $\Lambda \approx 68^\circ$  (above the magenta solid curve, which is repeated in subsequent panels for reference). Just after the shock, as seen in the SECS panel B, eastward currents became enhanced at almost all longitudes at  $\Lambda$ 's below the solid magenta line to the lowest  $\Lambda$  of observation ( $\sim 42^\circ$ ). A dashed magenta line outlines this region. This panel shows the ionospheric currents of the enhanced penetrating electric fields seen by the radars, as expected, and also shows that they extended to much lower latitudes than could be seen by the radars. The mid-latitude currents returned to near their pre-shock configuration level during the northward IMF interval between periods 1 and 2 (panel C). They then increased again during southward IMF period 2 (panels D and E), indicating that the penetrating electric field pattern during period 2 was similar to that during period 1. At higher latitudes, the dawnside DP2 current cell, as well as the duskside cell, became visible over North America, as did the sunward current between the duskside and dawnside cells.

During the periods 3 and 4 of longitudinally narrow, bursty flows (panels F-I), the ionospheric equivalent currents became substantially different than during the previous intervals. In particular, longitudinal narrow regions of current appear to extend to the lowest  $\Lambda$  of observation. It should be noted, however, that there are an insufficient number of magnetometer stations to accurately discern the longitudinally dependent details of the current structure, particularly at  $\Lambda$ 's  $< 45^\circ$  where longitudinal coverage is limited. However, it is clear that the currents have more longitudinal structure than during the earlier periods, indicating that the associated longitudinally structured electric fields penetrated to  $\Lambda$ 's at least  $10^\circ$  equatorward of the equatorward boundary of auroral electron precipitation as seen by the DMSP spacecraft observations in Figure 2. Such electric fields have the potential for injecting particles to low L-shells during this storm main phase.

Figure 6 show the AMPERE magnetic perturbations observed along Iridium satellite trajectories during the 10 min intervals identified by blue dashed vertical lines (a-f) in the upper panel of Figure 5. Red and blue shadings give upward and downward FACs, respectively, obtained from the curl of fits to the magnetic perturbations [Waters *et al.*, 2001]. The currents are denoted as  $J_r$  since they are actually radial, being calculated from the curl on a spherical surface. It can be seen that field-aligned currents were weak just before the shock impact (panel a). A well-defined Region 1 (R1) and R2 FAC pair formed during the post-shock period 1 (panel b), the duskside R2 currents extending equatorward to  $\Lambda \sim 62^\circ$ , which is  $\sim 3^\circ$  equatorward of the equatorward boundary of electron precipitation during the period as seen by the DMSP boundaries in Figure 4, consistent with these being the downward currents that are driven by the partial ring current and give rise to SAPS. During the period of smoothly enhanced convection (period 2, panel c), the well defined R1 and R2 current system amplified, and

extended equatorward by  $\sim 1-2^\circ$ , which is similar to the equatorward expansion seen in the duskside DMSP spacecraft equatorward boundaries after period 2 but before period 3.

As with the ionospheric equivalent currents, the FACs became significantly different during period 3 (panels d-f) than at earlier times. While the current fitting procedure significantly smooths longitudinal variations, the current system near midnight changes from that of the typical R1-R2 system to one of multiple, smaller scale currents, consistent with the increased structuring seen in the electric fields and the ionospheric equivalent currents. The latitudinal structuring is most evident in the magnetic perturbation vectors, which exhibit multiple east-west reversals along one or more tracks near midnight. Significant magnetic perturbations extend to  $\Lambda \sim 52^\circ$  in panels e and f, which is where the sub-auroral bursts are seen in the radar data in Figure 4.

#### **4. Ionospheric densities revealed by vertical TEC and PFISR.**

TEC measurements at 21, 24, and 04 MLT from available ground GPS stations are shown in Figure 7 as a function of  $\Lambda$  and UT. Magenta dots identify the equatorward boundary of plasma sheet electron precipitation, based on precipitating electron energy flux of  $10^{10} \text{ ev}/(\text{cm}^2 \text{ ster-s})$ , and magenta circles give the poleward boundary of auroral particle precipitation (i.e., of electron precipitation, since its poleward boundary was at or poleward of the proton boundary). Magenta bars extending to lower latitudes give the equatorward boundary of less-intense, but detected, plasma sheet proton ( $<23$  MLT) or soft electron ( $>23$  MLT) precipitation, which extended to somewhat lower latitudes than did the main plasma sheet electron precipitation.


TEC values were low prior to the shock impact, and there may have been a small increase at  $\Lambda \gtrsim 67^\circ$  after the shock. The largest TEC values are seen after  $\sim 07$  UT and appear as features that move equatorward from the highest latitude shown ( $\Lambda = 80^\circ$ ). This latitude appears to be

within the polar cap, several degrees poleward of the poleward boundary of the auroral oval as indicated by the DMSP measurements, the auroral observations in movie S1, and the poleward boundary of R1 field-aligned currents in Figure 6. However, we note that the poleward boundary of the oval is not very clear in the auroral images and that there are uncertainties in using the southern hemisphere DMSP values for the poleward boundary in the northern hemisphere. Thus there is some uncertainty in our determination of the auroral poleward boundary. The equatorward boundary of the TEC enhancements, which also represents the poleward boundary of the mid-latitude trough, moves equatorward after ~07 UT, in approximate agreement with what is seen for the auroral oval electron precipitation by DMSP and the auroral imagers, as has previously been reported by *Zou et al.* [2011]. Additionally, the equatorward boundary of the mid-latitude trough appears to move equatorward in the 24 MLT panel, although examination of the TEC at all MLT indicates this may be related to azimuthal motion of a longitudinal feature.

The equatorward moving TEC enhancement features, having the characteristics of polar cap patches, are seen within the auroral oval (based on being equatorward of the DMSP poleward boundaries) from ~0730 to ~1200 UT. Electron density and temperature profiles measured by PFISR (Figure 8) in the pre-midnight sector (1000-1115 UT) confirm the typical patch signatures (enhanced densities above 300 km and lower electron temperature than of the surrounding auroral features) as structures moving equatorward across the PFISR field-of-view. The clearest of these are identified by dashed diagonal lines. This roughly corresponds to southward IMF periods 3 and 4, during which convection was dominated by flow bursts. These density enhancement features appear to move from the polar cap to the auroral oval as has previously been seen by *Zhang et al.* [2013] and from simulation results by *Crowley et al.*



[1996]. That they occur during the period of flow bursts suggests that the enhancements are brought into the auroral oval by flow channels from the polar cap that cross the open-closed field line boundary and enter the plasma sheet. Such entry of polar cap flow bursts into the plasma sheet is now believed to be a common feature that leads to plasma sheet flow bursts, giving rise to auroral poleward boundary intensifications (PBIs) and streamers [*de la Beaujardière et al.*, 1994; *Lyons et al.*, 2011; *Nishimura et al.*, 2010; *Pitkänen et al.*, 2013; *Shi et al.*, 2012; *Zou et al.*, 2014], and would be expected to carry the TEC enhancements equatorward within the auroral oval.

Consistent with the TEC flux enhancements being transported equatorward by flow bursts, the radar flow vectors in Figure 8 show that equatorward flow bursts were seen by PFISR at  $\Lambda = 66-67.5^\circ$  a few minutes before the patches appeared in the densities along the local magnetic field line ( $\Lambda = 65.4^\circ$ , beam 12). To explore the possibility further, Figure 9 shows TEC and LOS flows along 4 radar beams. The beams were selected to maximize overlapping coverage of TEC measurements and radar echoes as well as to illustrate various features of interest, and each TEC measurement has been averaged over the 3 adjacent beams centered on the beam illustrated in the upper left hand corner. For each beam, thick horizontal dashed lines identify a  $\Lambda$  in both the LOS and TEC panels that has been selected to maximize overlapping flow burst and TEC enhancement coverage. Thinner dashed vertical lines give visually estimated times of the initiation of flow burst crossings of the  $\Lambda$   horizontal lines.

As seen in the auroral oval, flow bursts extend over several degrees of latitude as they move both equatorward and azimuthally through the plasma sheet. Thus apparent motion of TEC and flow burst features along a radar beam reflects how both their equatorward and azimuthal flow leads to crossing of that beam. If the TEC enhancements are carried by the flow bursts,

there should be an association between their crossing of the radar beam and that of the flow bursts. Such an association seems clear from the CVW west beams on the left side of Figure 8, which look north-northwestward. These beams give the best views of density structures having a beam crossing that moves equatorward with time, beam 11 having better TEC coverage and beam 14 having broader LOS velocity coverage. While there is not a precise one-to-one association between the flows and the TEC enhancements, there is a general association between the time intervals of flow bursts and of TEC enhancements (~0845-1215 UT). Furthermore, a TEC enhancement is seen near most of the locations where the vertical dashed lines (at  $\Lambda = 60^\circ$ ) crosses the horizontal dashed line, and most of TEC enhancements along the dotted line occur near these crossings.

FHW beam 8 looks northwestward and saw flow bursts having a beam crossing location that moved equatorward with time. The horizontal line shown in this panel is at  $\Lambda = 58^\circ$  and at a beam location a little more than 1 hr to the east of that for the line shown in the CVW panels. Similar features are seen as for the CVW beams, though with a more clear association between the two time periods of LOS flow and TEC enhancements, from ~9-10 and from ~11-12 UT, and the clear gap in between. The CVE beam looks east-northeastward, and thus sees the flow bursts as away from the radar flows (blue color) moving eastward in the dawn convection cell. The crossing of the radar beam by these flow bursts moves to higher latitudes (further range gates) with time, which reflects the bursts eastward motion within the dawn convection cell. The TEC enhancements also show such motion of their crossings of the radar beam to higher range gates. Furthermore, as with the FHW beam, there is clear association between the two regions on LOS flow and TEC enhancements and a clear gap in between. Both of these features along the CVE

beam support the suggestion that the TEC enhancements are carried with the auroral oval by the flow bursts.

Figures 7 - 9 give evidence that the flow bursts bring TEC enhancements from the polar cap into the plasma sheet. These enhancements are brought further and further equatorward during periods 3 and 4 to near the equatorward boundary of the auroral, and this occurs at the same as the flow bursts also expand the auroral oval equatorward to  $\Lambda_{\text{eq}}$  below  $55^\circ$ . We note that the evidence from Figures 7-9 is qualitative, so that it would be desirable develop a more quantitative comparison between the flow bursts and TEC enhancements. This would require taking into account the LOS nature of the Super DARN flow velocities and the tendency for high TECs to be associated with enhanced radar backscatter, a tendency that can be seen in Figure 8.

### **5. Ring current particle injection.**

The equatorward expansion of the auroral oval should correspond to an earthward motion of the inner edge of the plasma sheet. The plasma sheet particles, energized with the increasing magnetic field strength as the flow bursts move them earthward, should be expected to become part of the storm time ring current. We examine this possibility by examining the equatorial Van Allen Probes (VAP) particle observations. VAP-B preceded VAP-A as they both moved inbound in the post-midnight sector and outbound in the pre-midnight sector.

Figure 10 shows time profiles of electrons and ions measured by the MagEIS instrument [Blake *et al.*, 2013] from the last VAP pass (VAP-B outbound) before the storm shock impact (top), the next VAP-B and VAP-A passes (inbound and outbound) during the storm main phase (middle), and the subsequent inbound and outbound passes during the beginning of the storm recovery phase (bottom). The quiet time passes show the typical quiet time structure of the ring current ions, their outer zone peak moving earthward with increasing energy, and of the

ring current and radiation belt electrons with their two-zone structure. The flux enhancement due to the 06 UT shock impact was seen at  $L \approx 6$  on the VAP-B inbound pass.

On each post shock pass, the inner edge of ion injection as seen in the line plots is identified with a solid maroon line, and the location of the plasma pause based on the density measurements (inferred from the upper hybrid resonance line using the EMFISIS wave measurements [Kletzing *et al.*, 2013; Kurth *et al.*, 2015]) is identified by a dotted dark-green line. The electron data show approximate correspondence between their inner injection boundary and that of the ions. On the first VAP-B inbound pass, the ion injection edge and the plasma pause can be seen at ~0730-0800, just after period 2. They were located at  $L = 4.2$  and  $3.5$ , respectively, which is somewhat earthward from their typical quiet time location. The subsequent VAP-A pass observed the boundaries at ~09-0930 UT, and shows that they had moved  $\sim 0.7 R_E$  further earthward during the first half of period 3. As seen in the profile for the outbound portions of these passes, and additional  $\sim 0.9 R_E$  of inward motion was seen for the ion inner edge during the remainder of period 3. However, some of this later inward motion was likely an MLT effect from particle drift trajectories, as can be seen by the ion edge being earthward of the plasma pause on the duskside. The recovery phase orbit shows that a further few tenths of an  $R_E$  earthward penetration occurred during, or somewhat after, the flow burst period 4. Similar locations for the inner edge of ion injection can be seen in Figure 3 of Gkioulidou *et al.* [2014], where it is also seen that the peak in ring current pressure moved in to  $L \sim 3.5$ , consistent with what is expected for a storm of the strength [e.g., Antonova, 2006; Antonova and Stepanova, 2015]

Each observed L-value was mapped to  $\Lambda$  using a dipole field (which is valid at these low L's). The corresponding  $\Lambda$ 's are shown by magenta X's for the ion edges and P's for

the plasmopause in Figure 4, with the addition of the corresponding  $\Lambda$ 's from the equatorial THEMIS spacecraft given by brown X's and P's. Values from duskside (dawnside) portions of spacecraft orbits are shown in the more duskside CVW panel (beams 17,19,20) and the more dawnside THE panel, respectively. The MLT of each observation point is also indicated.

Very near the time of the shock impact, the THEMIS spacecraft showed the boundaries laying a few degrees equatorward of the DMSP electron precipitation boundaries, likely representing previous weak activity. Based on the dawnside THEMIS and VAP passes, little equatorward motion was seen during periods 1 and 2, with most of the equatorward motion of the boundaries occurring during period 3. This is consistent with what is seen in the DMSP boundaries, the radar echo boundaries, and the auroral observations. These observations indicate that the large majority of the injections of ring current particles to lower L occurred during the flow-burst time period of most rapid and furthest equatorward penetration of the auroral oval and associated currents. This inference is consistent with observations [Gkioulidou *et al.*, 2014] and modeling [Yu *et al.*, 2014] of this storm that indicate the importance of multiple ion injections to the formation of the ring current during the storm main phase.

## 6. Summary

Taking advantage of the excellent coverage of the 2013 March 17 storm main phase from ground-based instruments and from low- and high-altitude spacecraft, we have evaluated the driving of fundamental main-phase phenomena and found evidence for common driving of the auroral oval, nightside ionospheric currents, the R2 field-aligned current system, ionospheric densities, and injection of particles to form the storm time ring current. The storm shock impact drove activity almost immediately: dramatic poleward expansion of the poleward boundary of the auroral oval, strong auroral activity, and strong penetrating mid-latitude convection and

ionospheric currents. Equatorward expansion of the auroral oval was limited. The dramatic poleward expansion, which implies rapid reconnection along the night side polar cap boundary, is associated with a broad, active region of new plasma sheet with high proton energies that appears to have formed within a region of previously open lobe field lines. Additionally, a very large increase in the mid-latitude, sub-auroral westward electric fields was observed.

After the initial ~15 min period 1 of southward IMF, there was a less active ~15 min period of northward IMF and then a second period of southward IMF that lasted for ~45 min. The auroral observations showed an equatorward penetration of the oval by  $\sim 3^\circ$  to  $\Lambda \sim 66^\circ$  during this period 2. After decreasing substantially during the preceding northward IMF period, there was a very large increase in the mid-latitude, sub-auroral westward flows during period 2. While the flow speeds were similar to those seen during period 1, the flow had far less structuring during period 2 and this difference between the two periods is reflected in the auroral observations.

Convection became very different during the ~4 hr time of southward IMF of periods 3 and 4. Very bursty flows were observed, with LOS speeds varying from ~500 m/s to close to 0 m/s repetitively over ~10-20 min periods. The flow bursts had a strong equatorward component, and appeared to turn azimuthally as would be expected from a guiding by the large-scale convection pattern. Some of the bursts within the dusk convection cell appear to have penetrated equatorward of the electron plasma sheet, becoming bursts of enhanced flows that were seen in the SANS region. Auroral streamers were seen throughout the first ~2 hours of this period, after which the ASIs with good viewing rotated too far toward the morning section to see streamers. The equatorward boundary of the observed aurora moved rapidly equatorward, from  $\Lambda \sim 66^\circ$  to  $\Lambda \sim 60^\circ$ , as seen in the PINA keogram. Based on the radar echo locations and the DMSP electron

precipitation observations, the oval continued to expand to  $\Lambda \sim 55^\circ$  during the first two hours of this southward IMF interval but did not subsequently expand further.

The above three different modes of electric field occurred following the storm shock and during the storm main phase and were identified using the radar and auroral observations. We have found that the different modes were reflected in the ionospheric and field-aligned current systems. Enhancement of the DP2 and R2 current system were seen during period 1 and became strongly enhanced during period 2. Similar penetration of the ionospheric currents to mid-latitudes was seen during both periods. During periods 3 and 4, when nightside convection consisted of strong bursts with significant spatial structure, both current systems changed from their earlier typical patterns associated with large-scale convection to patterns reflecting the enhanced structure of the electric fields. Also, the currents continued to intensify, the region of strong currents continued to expand equatorward with the auroral oval, and penetrating ionospheric currents continued but with substantial enhanced spatial structure.

The different driving modes were also reflected in the ionospheric densities obtained from vertical TEC measurements. The equatorward boundary of the TEC enhancements, which also represents the poleward boundary of the mid-latitude trough, moved equatorward most rapidly after  $\sim 07$  UT, in approximate agreement with what is seen for the auroral oval electron precipitation, the equatorward motion being the most rapid during approximately the first half of period 3. Furthermore, the TEC measurements showed large equatorward moving enhancement features within the auroral oval during periods 3 and 4 of bursty convection, some of which were traceable over  $\sim 25\text{-}30^\circ$  of latitude. Simultaneous TEC and radar flow measurements suggest that the TEC enhancements were brought into the auroral oval from the polar cap, and subsequently

moved equatorward and azimuthally within the auroral oval, due to their being carried by the flow bursts as they move from the polar cap to the plasma sheet and then within the plasma sheet.

The earthward injection of particles to form the storm time ring current was found to correspond well with the period of most rapid and furthest equatorward penetration of the auroral oval and associated currents that was associated with bursty convection.

## 7. Conclusions

In conclusion, during the course of the storm expansion phase, the radar observations indicated the existence of three different southward IMF modes of electric fields that drove storm time phenomena. These three modes were reflected in the aurora, and in ionospheric and field-aligned current. Poleward expansion of auroral oval, which indicates rapid nightside reconnection, occurred primarily during the first driving period, which initiated immediately after the shock impact. Equatorward expansion of the auroral oval occurred predominantly during the period of the third driving mode, when the electric field became extremely bursty with much spatial structure, this structure being reflected by equatorward extending auroral streamers and highly structured ionospheric and field-aligned currents. This also approximately corresponded to the time period of the largest equatorward motion of the ionospheric trough, the biggest earthward injection of ions and electrons into the ring current, and equatorward and azimuthally moving high TEC features within the auroral oval that appear to come from the polar cap. This indicates a common driving of all these storm time features, which are often considered separately. Why the electric field enhancements had these three different manifestations, and why the bursty enhancement interval was more effective in driving storm phenomena is not clear from our analysis of this one storm. Coordinated and simultaneous multi-instrument observations of main phase phenomena for additional storms would allow for



evaluating the generality of the results presented here, and they might also help us understand why certain driving conditions may be more effective than others.

## Acknowledgements

Work at UCLA has been supported by NSF grant 1401822 and NASA grants NNX15AD08G and NNX15AF61G. S. Zou is supported by NSF grants AGS1400998 and AGS1342968. SuperDARN is a collection of radars funded by national scientific funding agencies of Australia, Canada, China, France, Japan, South Africa, United Kingdom and United States of America. JMR acknowledges the support of NSF under award AGS-1341918. The SuperDARN data can be obtained from JMR or viewed using the Virginia Tech SuperDARN website at <http://vt.superdarn.org/>. SGS acknowledges support from NSF under award AGS-1341925. The DMSP data are maintained by the Air Force Research Laboratory and Applied Physics Laboratory at Johns Hopkins University. CIGO magnetometer data is from the University Alaska magnetometer array. We thank I.R. Mann, D.K. Milling, and the CARISMA for the CARISMA magnetometer data, which is from the University of Alberta and funded by the Canadian Space Agency. OMNI data were downloaded from cdaweb. We thank the AMPERE team and the AMPERE Science Center for providing the Iridium derived data products. We thank the SuperMAG, PI Jesper W. Gjerloev for make the SuperMAG indices available at <http://supermag.jhuapl.edu/>. The Poker Flat Incoherent Scatter Radar is operated by SRI International on behalf of the US National Science Foundation under NSF Cooperative Agreement AGS-1133009, and the data is available at <http://amir.com/amir/links/data-access/>. We thank M. Nicholls and M. McCready

for their assistance with this radar data. The Van Allen Probes data from EMFISIS were obtained from <https://emfisis.physics.uiowa.edu/data/index>, the MagEIS data from [http://www.rbsp-ect.lanl.gov/data\\_pub/](http://www.rbsp-ect.lanl.gov/data_pub/), and the THEMIS data from <http://themis.ssl.berkeley.edu/themisdata/>. We acknowledge NASA contract NAS5-02099 for use of data from the THEMIS Mission. Specifically: J. W. Bonnell and F. S. Mozer for use of EFI data, J. P. McFadden for use of ESA data, and, for the ASI, we thank S. Mende, the CSA for logistical support in fielding and data retrieval from the GBO stations, and NSF for support of GIMNSS through grant AGS-1004736.

We thank the many different groups operating magnetometer arrays for providing data used in the SECS analysis: 1. AUTUMNX magnetometer network is funded through the Canadian Space Agency / Geospace Observatory (GO) Canada program, Athabasca University, Centre for Science / Faculty of Science and Technology, 2014; 2. The Canadian Magnetic Observatory Network (CANMON) is maintained and operated by the Geological Survey of Canada - <http://gsc.nrcan.gc.ca/geomag>; 3. Geophysical Institute Magnetometer Array operated by the Geophysical Institute, University of Alaska. More information about this data set is available at <http://magnet.asf.alaska.edu/>; 4. The Magnetometer Array for Cusp and Cleft Studies (MACCS) array is supported by US National Science Foundation grant ATM-0827903 to Augsburg College; 5. We would like to thank Anna Naemi Willer for calibrating the DTU magnetometers; 6. The McMAC Project is sponsored by the Magnetospheric Physics Program of National Science Foundation and maintained by Dr. Peter Chi. 7. The Solar and Terrestrial Physics (STEP) magnetometer file storage is at Department of Earth and Planetary Physics, University of Tokyo and maintained by Dr. Kanji Hayashi ([hayashi@gr1.s.u-tokyo.ac.jp](mailto:hayashi@gr1.s.u-tokyo.ac.jp)); 8. The USGS Geomagnetism Program.

All data is properly cited and referred to in the reference list or in the acknowledgements.

## References

- Crowley, G., Critical review of ionospheric patches and blobs, in *Review of Radio Science 1993–1996*, chapter 27, Ed. W.R., Stone, Oxford Science Publication, UK, 619–648, 1996.
- Amm, O., and A. Viljanen (1997), Ionospheric Elementary Current Systems in Spherical Coordinates and Their Application, *J. Geomagn. Geoelectr.*, 49(7), 947–955, doi:10.5636/jgg.49.947.
- Anderson, B. J., H. Korth, C. L. Waters, D. L. Green, V. G. Merkin, R. J. Barnes, and L. P. Dyrud (2014), Development of large-scale Birkeland currents determined from the Active Magnetosphere and Planetary Electrodynamics Response Experiment, *Geophys. Res. Lett.*, 41(9), 2014GL059941, doi:10.1002/2014GL059941.
- Angelopoulos, V. (2008), The THEMIS Mission, *Space Sci. Rev.*, 141(1–4), 5–34, doi:10.1007/s11214-008-9336-1.
- Antonova, E. E. (2006), Stability of the magnetospheric plasma pressure distribution and magnetospheric storms, *Adv. Space Res.*, 38(8), 1626–1630, doi:10.1016/j.asr.2005.05.005.
- Antonova, E. E., and M. V. Stepanova (2015), The problem of the acceleration of electrons of the outer radiation belt and magnetospheric substorms, *Earth Planets Space*, 67(1), 1–8, doi:10.1186/s40623-015-0319-7.
- Baker, D. N. et al. (2014), Gradual diffusion and punctuated phase space density enhancements of highly relativistic electrons: Van Allen Probes observations, *Geophys. Res. Lett.*, 41(5), 2013GL058942, doi:10.1002/2013GL058942.
- de la Beaujardière, O., L. R. Lyons, J. M. Ruohoniemi, E. Friis-Christensen, C. Danielson, F. J. Rich, and P. T. Newell (1994), Quiet-Time Intensifications Along the Poleward Auroral Boundary Near Midnight, *J. Geophys. Res.*, 99(A1), 287–298, doi:10.1029/93JA01947.
- Blake, J. B. et al. (2013), The Magnetic Electron Ion Spectrometer, *Space Sci. Rev.*, 179(1–4), 385–421, doi:10.1007/s11214-013-9991-8.
- Boudouridis, A. (2003), Effect of solar wind pressure pulses on the size and strength of the auroral oval, *J. Geophys. Res.*, 108(A4), doi:10.1029/2002JA009373. [online]

Available from: <http://www.agu.org/pubs/crossref/2003/2002JA009373.shtml> (Accessed 15 August 2010)

- Boudouridis, A., E. Zesta, L. Lyons, P. Anderson, and D. Lummerzheim (2004), Magnetospheric reconnection driven by solar wind pressure fronts, *Ann. Geophys.*, *22*(4), 1367–1378.
- Boudouridis, A., E. Zesta, L. R. Lyons, P. C. Anderson, and D. Lummerzheim (2005), Enhanced solar wind geoeffectiveness after a sudden increase in dynamic pressure during southward IMF orientation, *J. Geophys. Res. Space Phys.*, *110*(A5), A05214, doi:10.1029/2004JA010704.
- Crowley, G., Critical review of ionospheric patches and blobs, in *Review of Radio Science 1993–1996*, chapter 27, Ed. W.R., Stone, Oxford Science Publication, UK, 619–648, 1996.
- Gjerlov, J. W. (2012), The SuperMAG data processing technique, *J. Geophys. Res. Space Phys.*, *117*(A9), A09213, doi:10.1029/2012JA017683.
- Gkioulidou, M., A. Ukhorskiy, D. G. Mitchell, T. Sotirelis, B. Mauk, and L. J. Lanzerotti (2014), The role of small-scale ion injections in the buildup of Earth's ring current pressure: Van Allen Probes observations of the March 17th, 2013 storm, *J. Geophys. Res. Space Phys.*, 2014JA020096, doi:10.1002/2014JA020096.
- Hori, T., A. Shinbori, N. Nishitani, T. Kikuchi, S. Fujita, T. Nagatsuma, O. Troshichev, K. Yumoto, A. Moiseyev, and K. Seki (2012), Evolution of negative SI-induced ionospheric flows observed by SuperDARN King Salmon HF radar, *J. Geophys. Res. Space Phys.*, *117*(A12), A12223, doi:10.1029/2012JA018093.
- Hudson, M. K., J. Paral, B. T. Kress, M. Wiltberger, D. N. Baker, J. C. Foster, D. L. Turner, and J. R. Wygant (2015), Modeling CME-shock-driven storms in 2012–2013: MHD test particle simulations, *J. Geophys. Res. Space Phys.*, *120*(2), 2014JA020833, doi:10.1002/2014JA020833.
- Kauristie, K., V. A. Sergeev, O. Amm, M. V. Kubyshkina, J. Jussila, E. Donovan, and K. Liou (2003), Bursty bulk flow intrusion to the inner plasma sheet as inferred from auroral observations, *J. Geophys. Res. Space Phys.*, *108*(A1), 1040, doi:10.1029/2002JA009371.
- Kikuchi, T., S. Tsunomura, K. Hashimoto, and K. Nozaki (2001), Field-aligned current effects on midlatitude geomagnetic sudden commencements, *J. Geophys. Res. Space Phys.*, *106*(A8), 15555–15565, doi:10.1029/2001JA900030.
- Kletzing, C. A. et al. (2013), The Electric and Magnetic Field Instrument Suite and Integrated Science (EMFISIS) on RBSP, *Space Sci. Rev.*, *179*(1–4), 127–181, doi:10.1007/s11214-013-9993-6.
- Kurth, W. S., S. De Pascuale, J. B. Faden, C. A. Kletzing, G. B. Hospodarsky, S. Thaller, and J. R. Wygant (2015), Electron densities inferred from plasma wave spectra obtained by the

Waves instrument on Van Allen Probes, *J. Geophys. Res. Space Phys.*, 120(2), 2014JA020857, doi:10.1002/2014JA020857.

Li, W. et al. (2014), Radiation belt electron acceleration by chorus waves during the 17 March 2013 storm, *J. Geophys. Res. Space Phys.*, 119(6), 2014JA019945, doi:10.1002/2014JA019945.

Li, Z., M. Hudson, B. Kress, and J. Paral (2015), Three-dimensional test particle simulation of the 17–18 March 2013 CME shock-driven storm, *Geophys. Res. Lett.*, 42(14), 2015GL064627, doi:10.1002/2015GL064627.

Lyons, L. R. et al. (2015), Azimuthal flow bursts in the inner plasma sheet and possible connection with SAPS and plasma sheet earthward flow bursts, *J. Geophys. Res. Space Phys.*, 2015JA021023, doi:10.1002/2015JA021023.

Lyons, L. R., Y. Nishimura, H.-J. Kim, E. Donovan, V. Angelopoulos, G. Sofko, M. Nicolls, C. Heinselman, J. M. Ruohoniemi, and N. Nishitani (2011), Possible connection of polar cap flow to pre- and post-substorm onset PBIs and streamers, *J. Geophys. Res.*, 116, 14 pp., doi:10.1029/2011JA016850.

Mauk, B. H., N. J. Fox, S. G. Kanekal, R. L. Kessel, D. G. Sibeck, and A. Ukhorskiy (2013), Science Objectives and Rationale for the Radiation Belt Storm Probes Mission, *Space Sci. Rev.*, 179(1–4), 3–27, doi:10.1007/s11214-012-9908-y.

Mende, S. B., S. E. Harris, H. U. Frey, V. Angelopoulos, C. T. Russell, E. Donovan, B. Jackel, M. Greffen, and L. M. Peticolas (2008), The THEMIS Array of Ground-based Observatories for the Study of Auroral Substorms, *Space Sci. Rev.*, 141(1–4), 357–387, doi:10.1007/s11214-008-9380-x.

Nishimura, Y. et al. (2010), Preonset time sequence of auroral substorms: Coordinated observations by all-sky imagers, satellites, and radars, *J. Geophys. Res.*, 115, doi:10.1029/2010JA015832. [online] Available from: <http://www.agu.org/pubs/crossref/2010/2010JA015832.shtml> (Accessed 26 March 2011)

Pitkänen, T., A. T. Aikio, and L. Juusola (2013), Observations of polar cap flow channel and plasma sheet flow bursts during substorm expansion, *J. Geophys. Res. Space Phys.*, 118(2), 774–784, doi:10.1002/jgra.50119.

Rideout, W., and A. Coster (2006), Automated GPS processing for global total electron content data, *GPS Solut.*, 10(3), 219–228, doi:10.1007/s10291-006-0029-5.

Shi, Y., E. Zesta, L. R. Lyons, J. Yang, A. Boudouridis, Y. S. Ge, J. M. Ruohoniemi, and S. Mende (2012), Two-dimensional ionospheric flow pattern associated with auroral streamers, *J. Geophys. Res.*, 117(A2), doi:10.1029/2011JA017110. [online] Available from: <http://www.agu.org/pubs/crossref/2012/2011JA017110.shtml> (Accessed 27 March 2012)

- Takahashi, N., Y. Kasaba, A. Shinbori, Y. Nishimura, T. Kikuchi, Y. Ebihara, and T. Nagatsuma (2015), Response of ionospheric electric fields at mid-low latitudes during sudden commencements, *J. Geophys. Res. Space Phys.*, 120(6), 2015JA021309, doi:10.1002/2015JA021309.
- Waters, C. L., B. J. Anderson, and K. Liou (2001), Estimation of global field aligned currents using the iridium® System magnetometer data, *Geophys. Res. Lett.*, 28(11), 2165–2168, doi:10.1029/2000GL012725.
- Weygand, J. M., O. Amm, A. Viljanen, V. Angelopoulos, D. Murr, M. J. Engebretson, H. Gleisner, and I. Mann (2011), Application and validation of the spherical elementary currents systems technique for deriving ionospheric equivalent currents with the North American and Greenland ground magnetometer arrays, *J. Geophys. Res. Space Phys.*, 116(A3), A03305, doi:10.1029/2010JA016177.
- Yu, Y., V. Jordanova, D. Welling, B. Larsen, S. G. Claudepierre, and C. Kletzing (2014), The role of ring current particle injections: Global simulations and Van Allen Probes observations during 17 March 2013 storm, *Geophys. Res. Lett.*, 41(4), 1126–1132, doi:10.1002/2014GL059322.
- Zesta, E. H., J. Singer, D. Lummerzheim, C. T. Russell, L. R. Lyons, and M. J. Brittnacher (2000), The Effect of the January 10, 1997, Pressure Pulse on the Magnetosphere-Ionosphere Current System, in *Magnetospheric Current Systems*, edited by S.-I. Ohnishi, R. Fujii, M. Hesse, and R. L. Lysak, pp. 217–226, American Geophysical Union. [online] Available from: <http://onlinelibrary.wiley.com/doi/10.1029/GM118p0217/summary> (Accessed 12 April 2015)
- Zhang, Q. H. et al. (2013), Direct Observations of the Evolution of Polar Cap Ionization Patches, *Science*, 339(6127), 1597–1600, doi:10.1126/science.1231487.
- Zou, S., L. R. Lyons, M. J. Nicolls, and C. J. Heinselman (2009), PFISR observations of strong azimuthal flow bursts in the ionosphere and their relation to nightside aurora, *J. Atmospheric Sol.-Terr. Phys.*, 71(6–7), 729–737, doi:10.1016/j.jastp.2008.06.015.
- Zou, S., M. B. Moldwin, A. Coster, L. R. Lyons, and M. J. Nicolls (2011), GPS TEC observations of dynamics of the mid-latitude trough during substorms, *Geophys. Res. Lett.*, 38(14), doi:10.1029/2011GL048178. [online] Available from: <http://europa.agu.org/?view=article&uri=/journals/gl/gl1114/2011GL048178/2011GL048178.xml&t=gl,2011,zou> (Accessed 17 August 2011)
- Zou, Y., Y. Nishimura, L. R. Lyons, E. F. Donovan, J. M. Ruohoniemi, N. Nishitani, and K. A. McWilliams (2014), Statistical relationships between enhanced polar cap flows and PBIs, *J. Geophys. Res. Space Phys.*, 119(1), 2013JA019269, doi:10.1002/2013JA019269.

# Author Manuscript

Figure 1: From top to bottom, the WIND  $P_{dyn}$ , the OMNI IMF, the SuperMAG upper U and lower L magnetic index, the SuperMAG ring current index for all MLT and within the dusk, noon, dawn, and midnight sectors, and ground magnetometer observations from North American stations near  $66-67^{\circ}$  MLAT with increasing UT of midnight (indicated by small vertical arrows) from CARISMA and the University of Alaska. N and E directions are local magnetic north and east, respectively, and Z-direction is vertically down. The IMF and  $P_{dyn}$  data are shifted so that the shock impact time agrees with the 0600 UT impact time seen by the ground magnetometers. Maroon dashed boxes identify four main periods of southward IMF seen after the shock arrival.

Figure 2: Representative snapshots from Movie S1. Each panel shows auroral images overlaid with LOS flow velocities from the SuperDARN radars. The images are mergers from all available ASIs over Canada and Alaska, and, from west to east, LOS flow velocities are from the midlatitude CVW, CVE, FHW, and FHE radars. Occasional radar echoes seen in the polar cap region are from the radar at Rankin Inlet. ASI station locations are given in the first panel. Yellow arrows in the upper and middle panels illustrate the magnitude of midlatitude westward flow. Pink and white arrows in the bottom panels identify longitudinally localized flow bursts seen in LOS flows directed toward a radar and eastward flow bursts seen in the easternmost radar echoes. Short white lines in the 0919 and 0920 UT panels illustrate the westward excursion of the western edge of a flow burst near midnight.

Figure 3: DMSP F17 and F16 observations several minutes before and several minutes after, respectively, the shock impact. For each spacecraft, integrated precipitating electron energy flux is shown in the top panel and energy-time spectrograms of precipitating



electron and ion energy flux are shown in the lower two panels. Latitudes of poleward and equatorward boundaries are given, and a region of weak polar cap arc precipitation is identified.

Figure 4: Overviews of the ASI and radar data from 05-1430 UT. Top 2 panels give keograms along a magnetic meridian somewhat to the west (east) of the central meridian of the FISH (PINA) ASI. The imager fields-of-view are shown in Figure 2. Lower four panels of Figure 4 show LOS velocities of the mid-latitude radars that are averaged over 2-3 beams along the four directions shown in the insert in the top right corner. Heavy blue dots give the equatorward boundary of plasma sheet electron precipitation observed on southern hemisphere crossings by DMSP F16-F18 spacecraft, the MLT of observation given in blue above each dot. Mapped  $\Lambda$ 's for the inner edge of ion injection and the plasma pause location are shown with magenta and brown X's for the ion edges and P's for the plasma pause from the VAP and THEMIS spacecraft, respectively, in the equatorial plane. Maroon dashed boxes identify four main periods of southward IMF seen after the shock arrival. "Bndry" is abbreviation for "boundary".

Figure 5: Ionospheric equivalent currents over North America obtained from ground based magnetometers (locations given by yellow stars) calculated from SECS method. The top panel reproduces the poleward looking CVW panel from Figure 2, maroon dashed lines identify the four southward IMF periods, vertical magenta lines identifying the times of the SECS panels in the lower two rows, and blue dashed vertical lines identifying the times of the AMPERE panels in Figure 6. The pre-shock eastward current of the duskside DP2 cell in panel A lies at  $\Lambda$ 's above the magenta solid curve, which is repeated in subsequent panels for reference. In subsequent panels, a dashed magenta line outlines the

region of enhanced currents at  $\Lambda$ 's below the solid magenta line.

Figure 6: Magnetic perturbations observed along Iridium satellite trajectories during the 10 min intervals identified by blue dashed vertical lines (a-f) in the upper panel of Figure 5. Red and blue shadings give upward and downward radial current, respectively, obtained from the curl of fits to the magnetic perturbations.

Figure 7: TEC measurements at 21, 24, and 04 MLT from available ground GPS stations as a function of  $\Lambda$  and UT. Magenta dots identify the equatorward boundary of plasma sheet electron precipitation, based on precipitating electron energy flux of  $10^{10}$  eV/(cm<sup>2</sup>-ster-s), and magenta circles give the poleward of auroral particle precipitation. Magenta bars extending to lower latitudes give the equatorward boundary of less-intense, but detected, plasma sheet proton (<23 MLT) or soft electron (>23 MLT) precipitation, which extended to somewhat lower latitudes than did the main plasma sheet electron precipitation. Dashed diagonal lines identify the clearest equatorward moving TEC enhancement features. "Bndry" is abbreviation for "boundary".

Figure 8: FISR measurements on March 17 2013 as a function of magnetic latitude and universal time. (a) Nightside convection flow vectors with a measurement uncertainty <300 m/s. (b) Raw electron densities with no correction for Te/Ti or Debye length effects measured by beam 12 (upward along the magnetic field). Altitude is indicated on the left Y axis and magnetic latitude is indicated on the right Y axis. (c) Electron temperature measured by the beam 12 long pulse mode. Dashed magenta lines indicate the start of patches as marked by enhanced F-region densities above ~300 km with reduced Te, and the patch connection equatorially directed flow bursts.

Figure 9: TEC and LOS flows averaged over the 3 adjacent beams centered on the beam

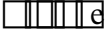
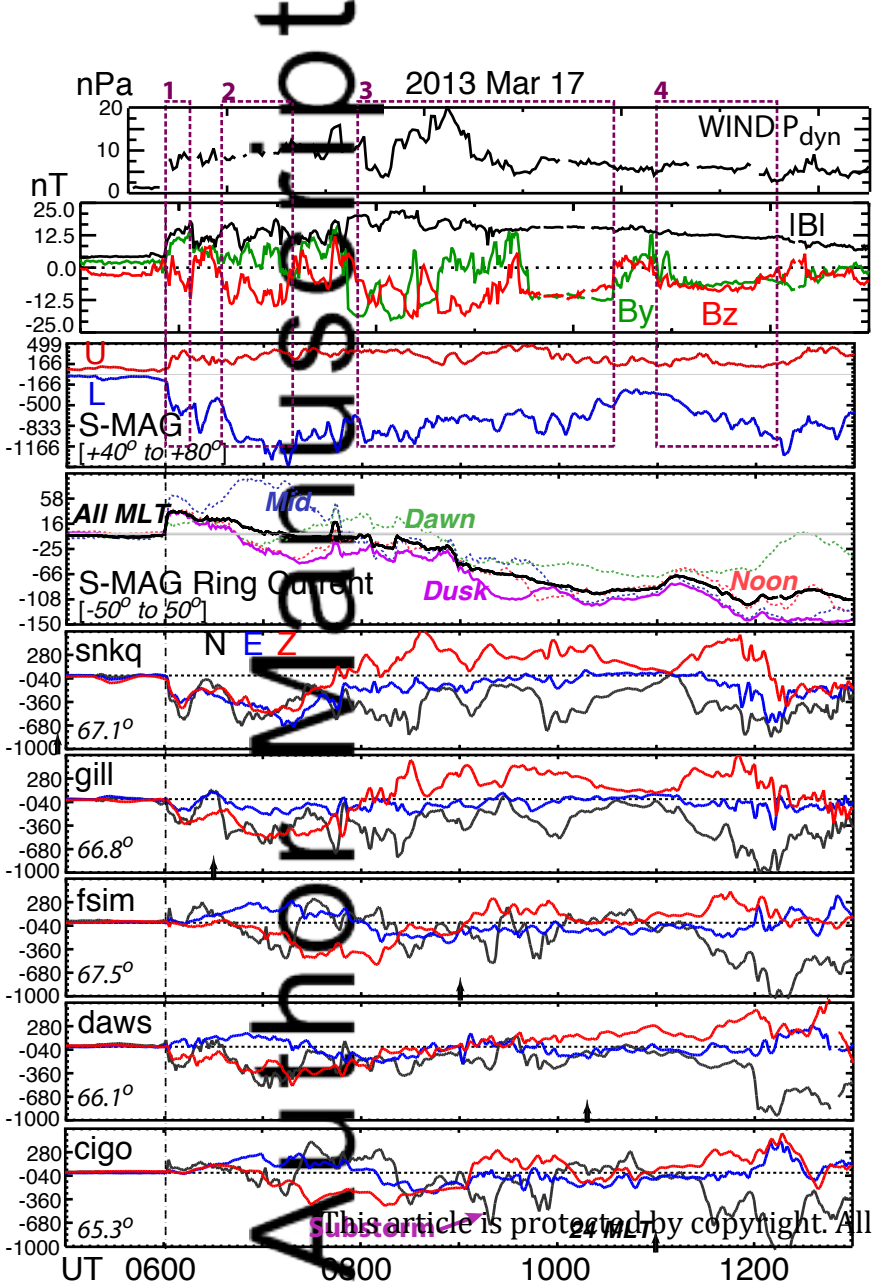
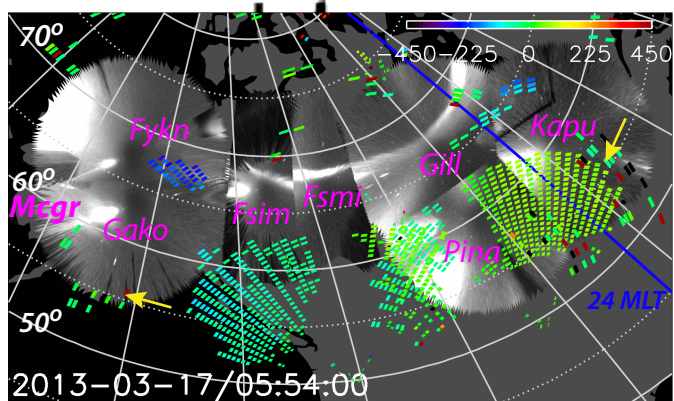
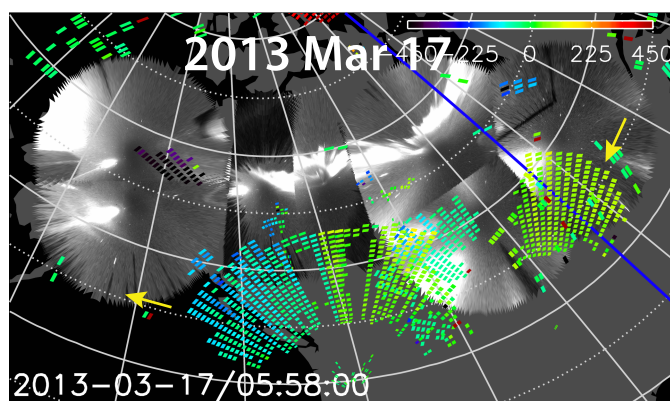
illustrated in the upper left hand corner. For each beam, thick horizontal dashed lines identify a  $\Lambda$  in both the LOS and TEC panels selected to maximize overlapping flow burst and TEC enhancement coverage. Thinner dashed vertical lines give visually estimated times of the initiation of flow burst crossings of the  $\Lambda$   horizontal lines.

Figure 10: Time profiles of electrons and ions from the last VAP pass (VAP-B outbound) before the storm shock impact (top), the next VAP-B and VAP-A passes (inbound and outbound) during the storm main phase (middle), and the subsequent inbound and outbound passes during the beginning of the storm recovery phase (bottom). On each post shock pass, the inner edge of ion injection as seen in the line plots is identified with a solid maroon line, and the location of the plasma pause based on the density measurements is identified by a dotted dark-green line. L-values and mapped  $\Lambda$ 's for each of these boundaries are identified.

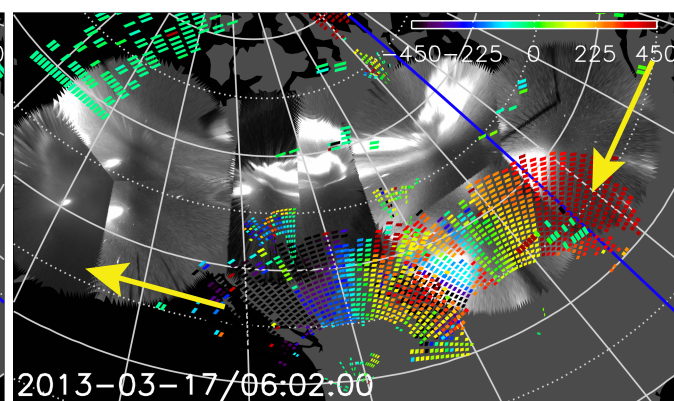




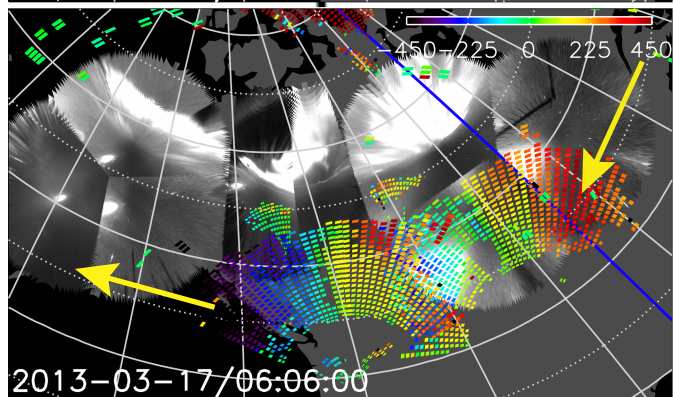
2013-03-17/05:54:00



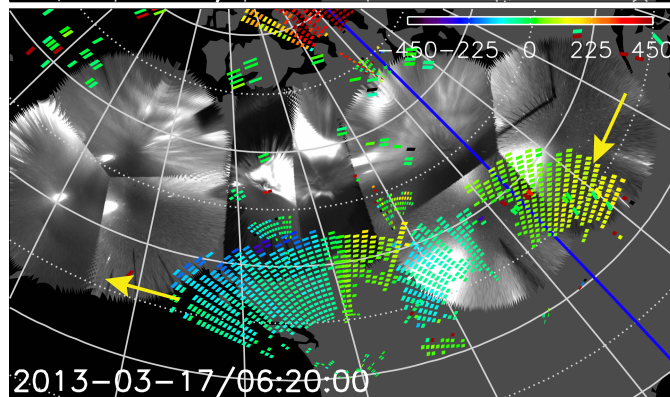
2013-03-17/05:58:00



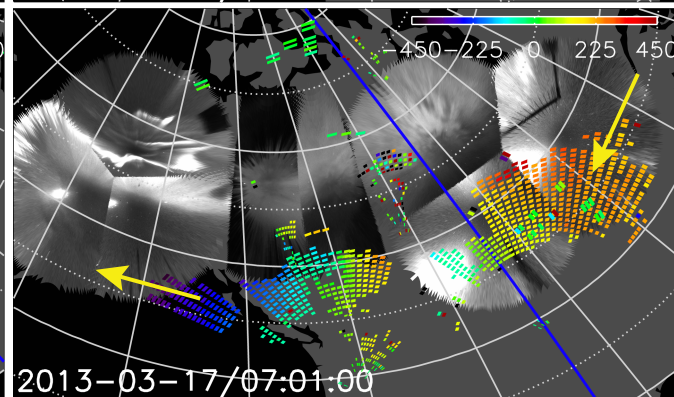
2013-03-17/06:02:00



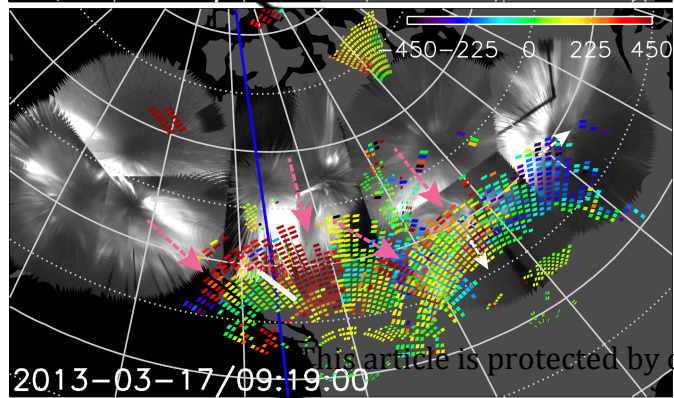
2013-03-17/06:06:00



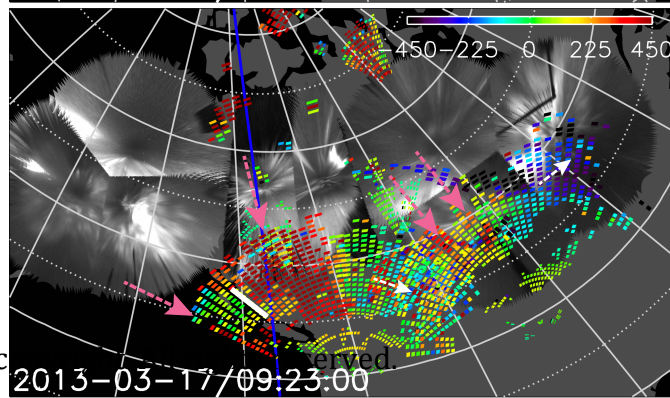
2013-03-17/06:20:00



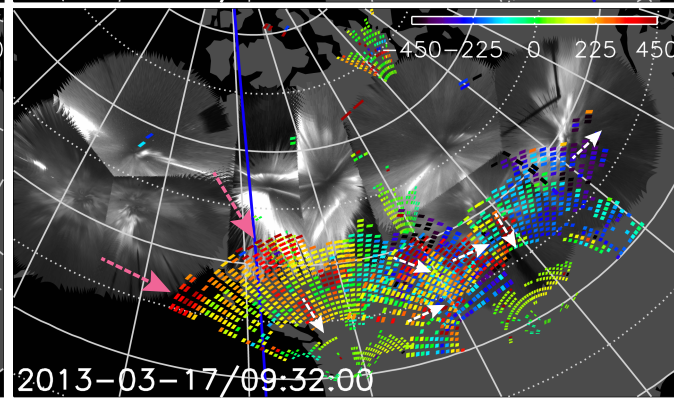
2013-03-17/07:01:00



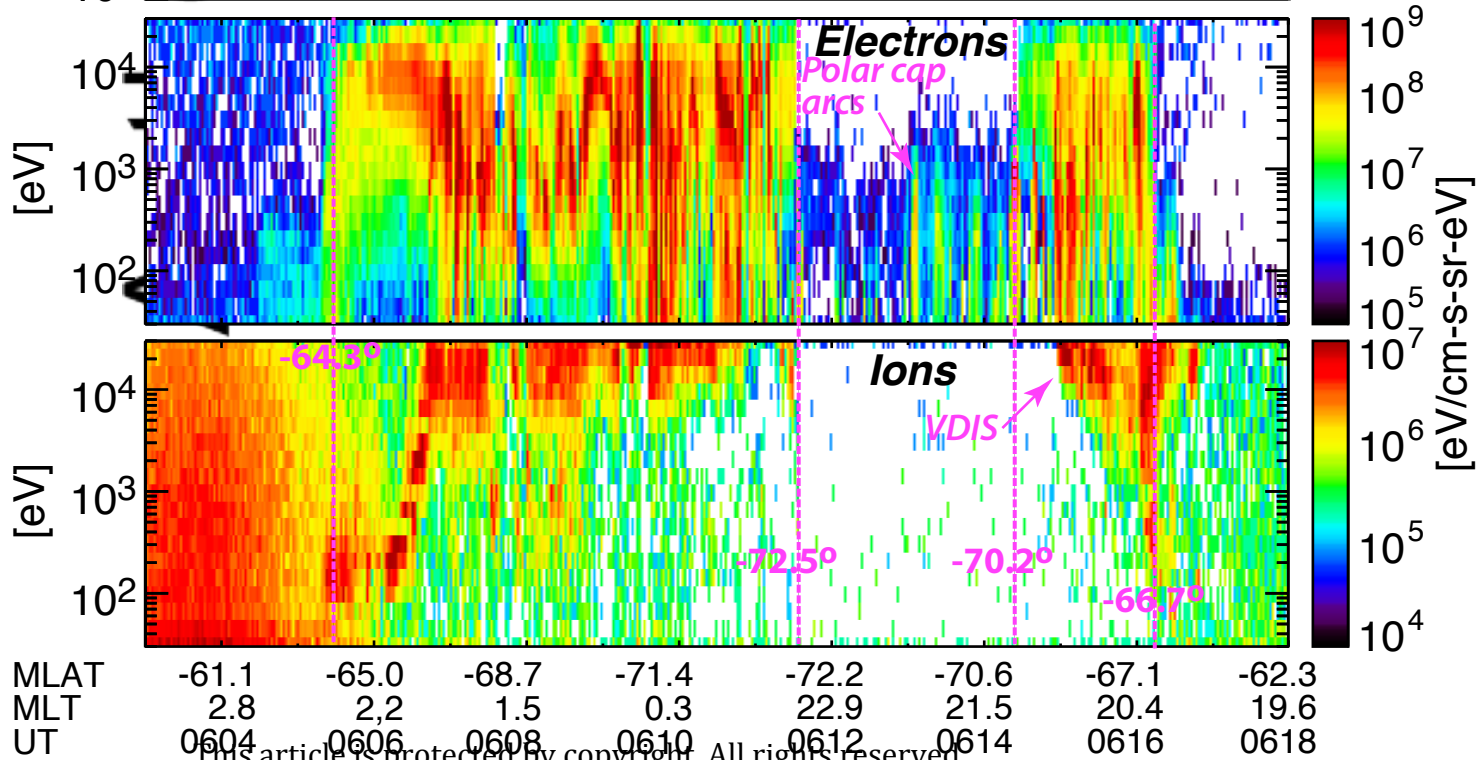
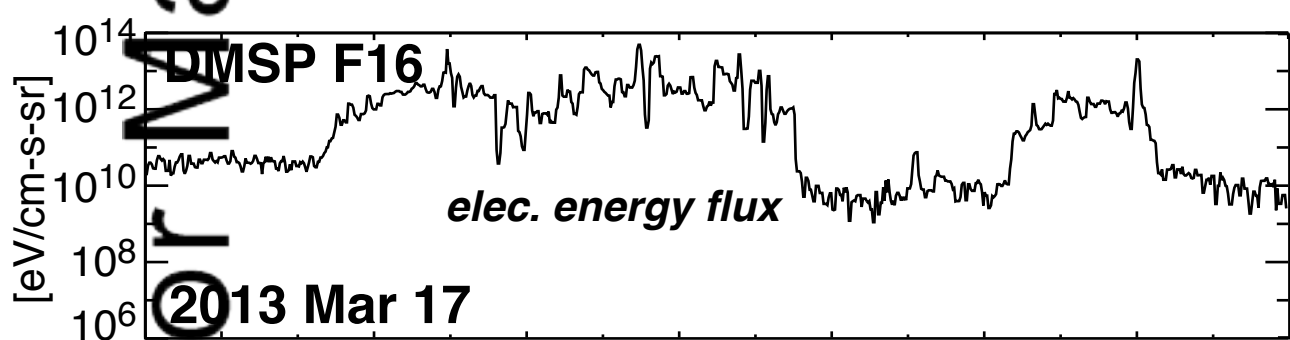
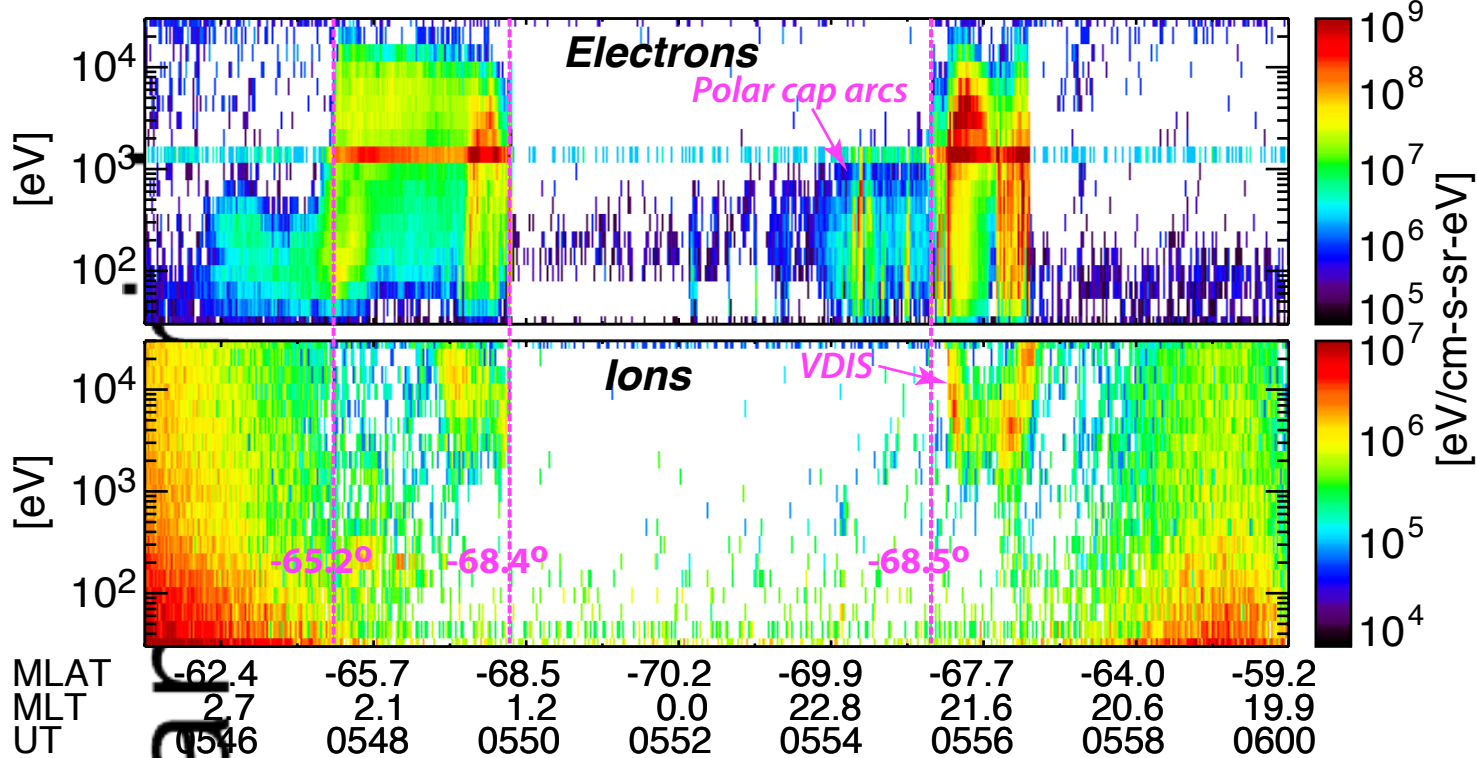
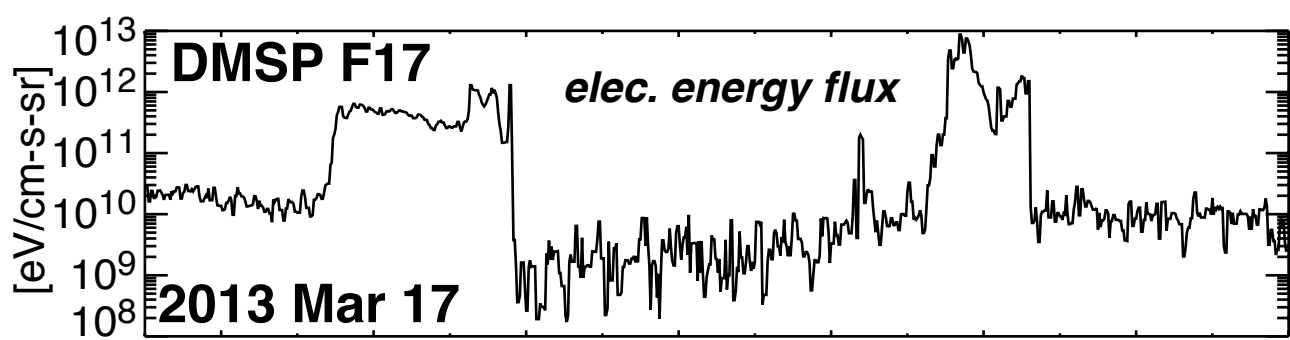
2013-03-17/09:19:00

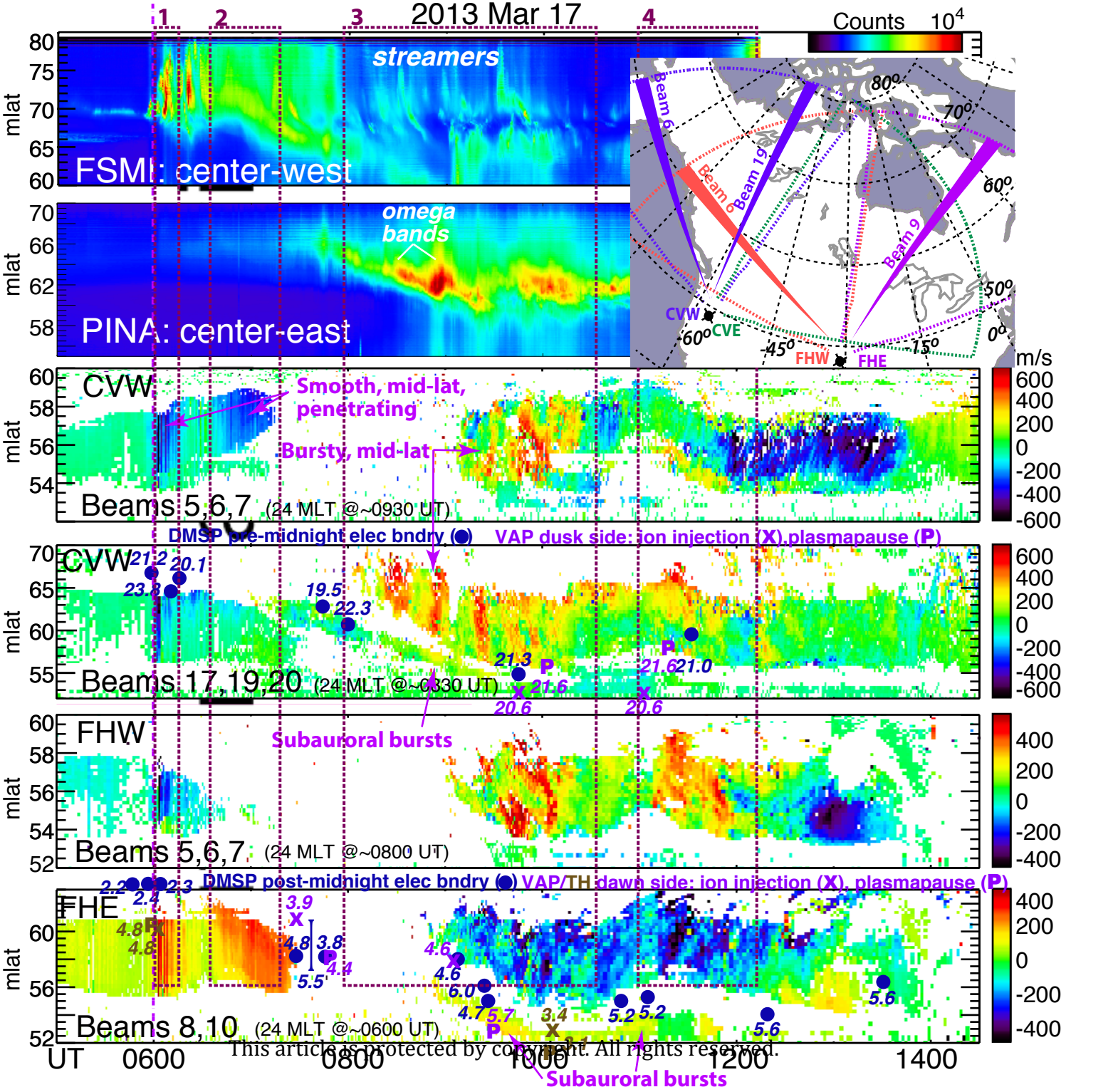


2013-03-17/09:23:00

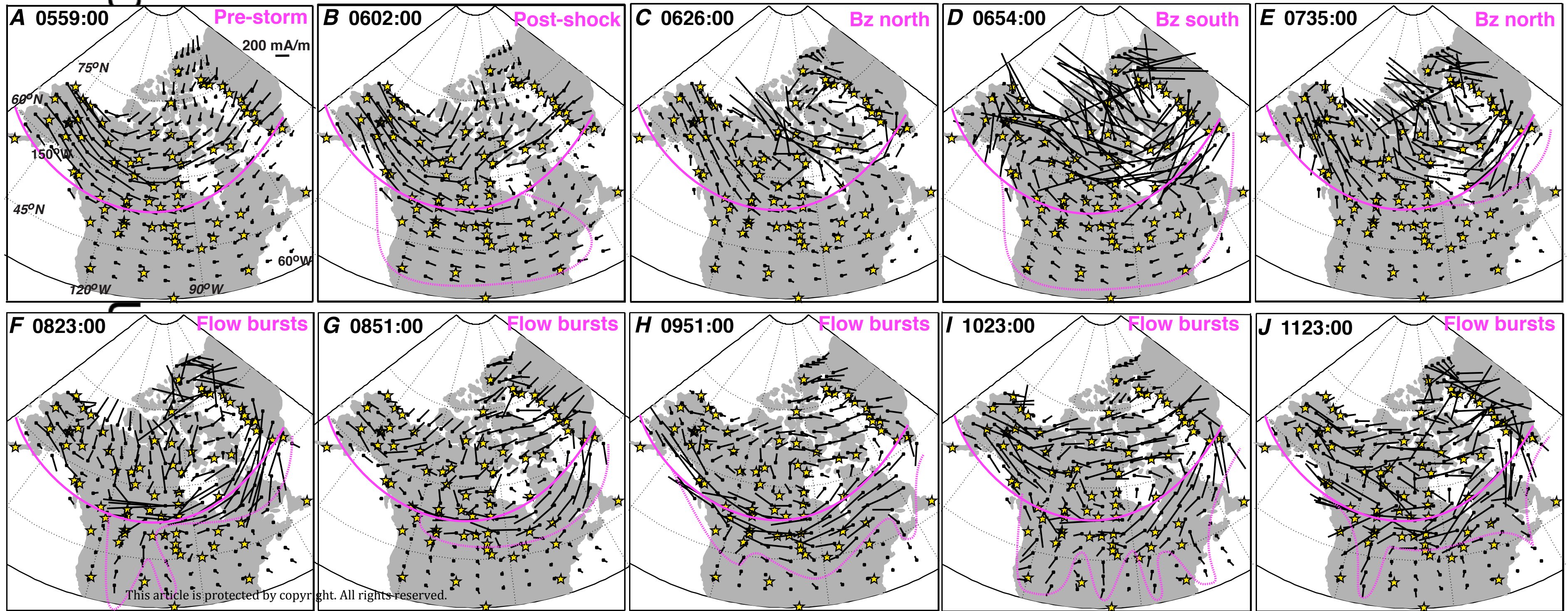
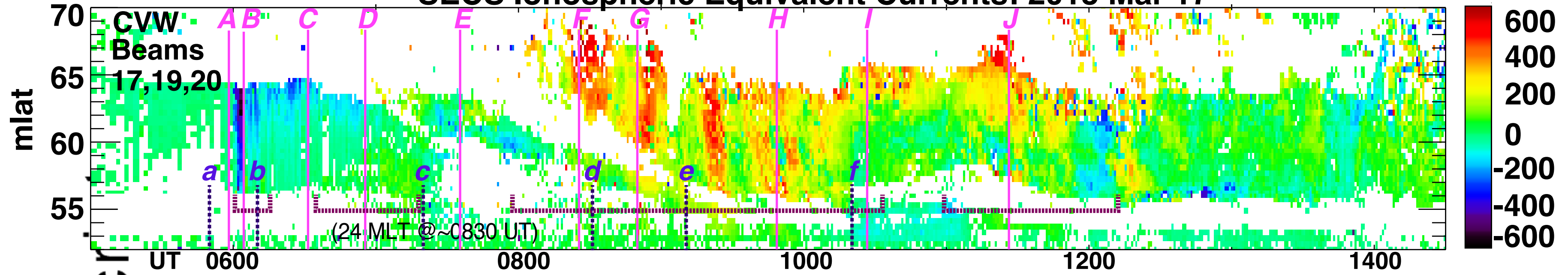


2013-03-17/09:32:00



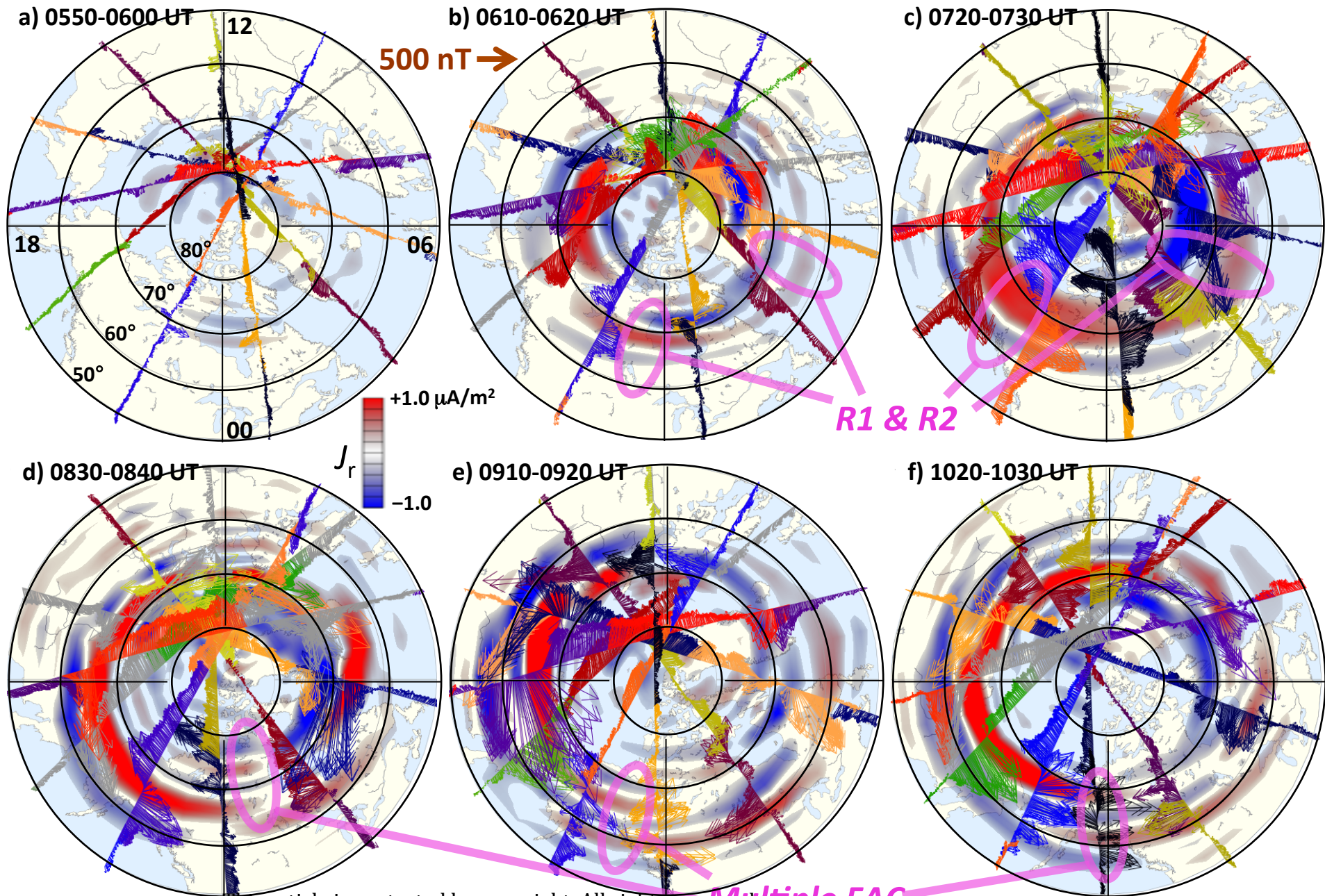


# SECS Ionospheric Equivalent Currents: 2013 Mar 17

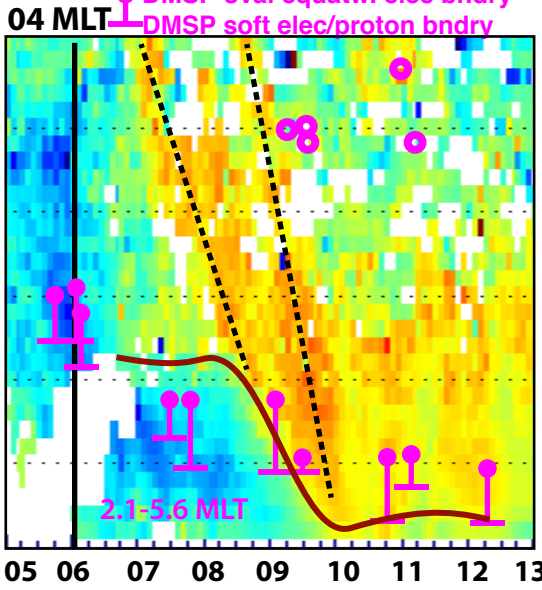
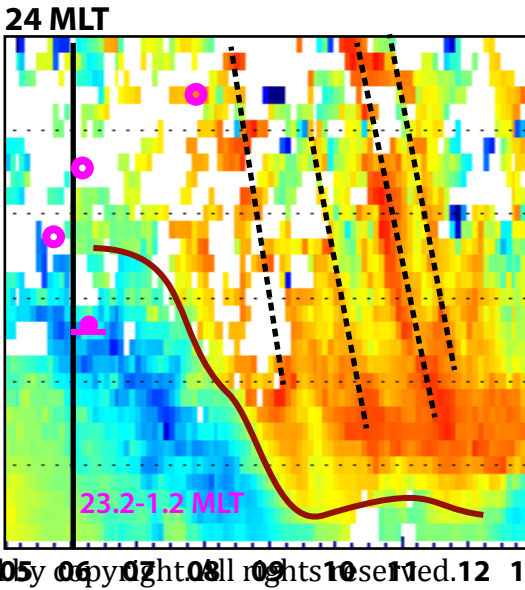
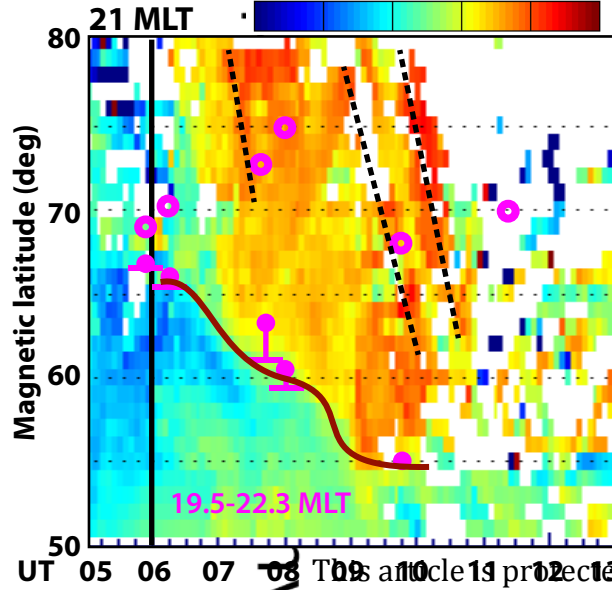
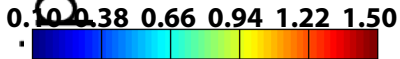




# AMPERE: 17 Mar 2013



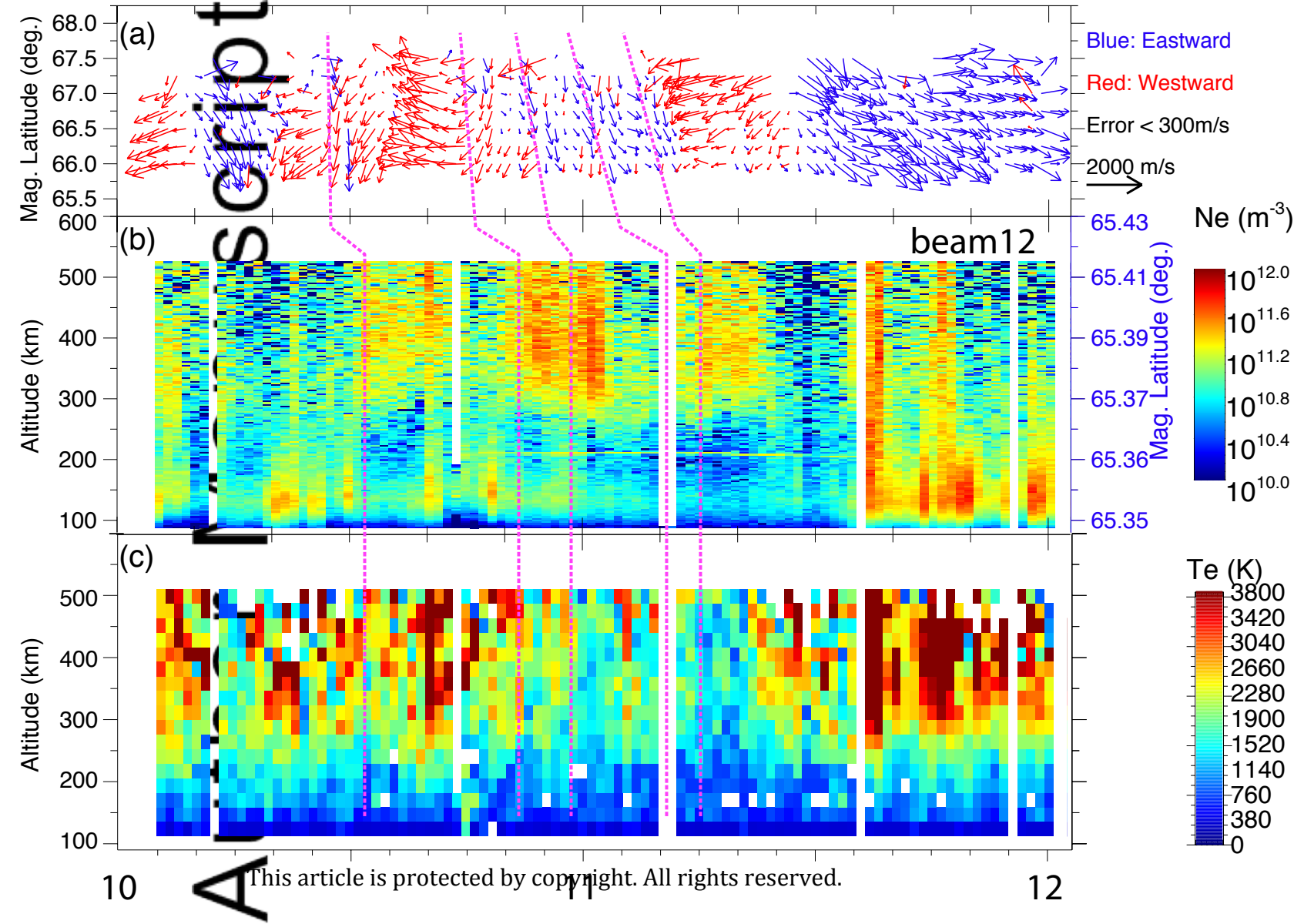
# GPS TEC (log 10) 2013 Mar 17

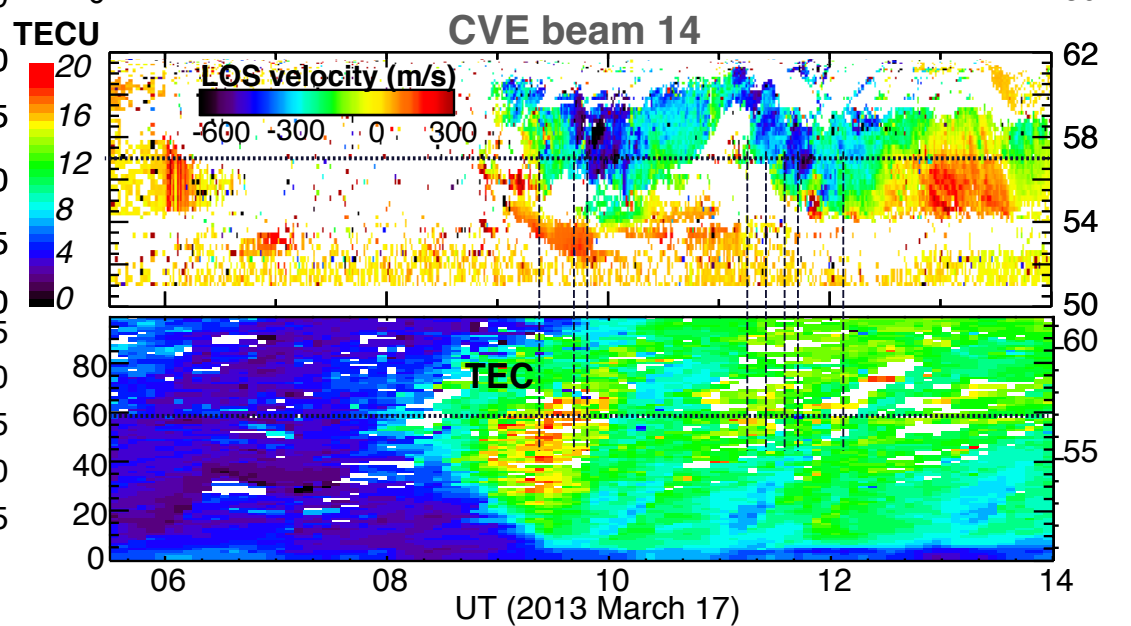
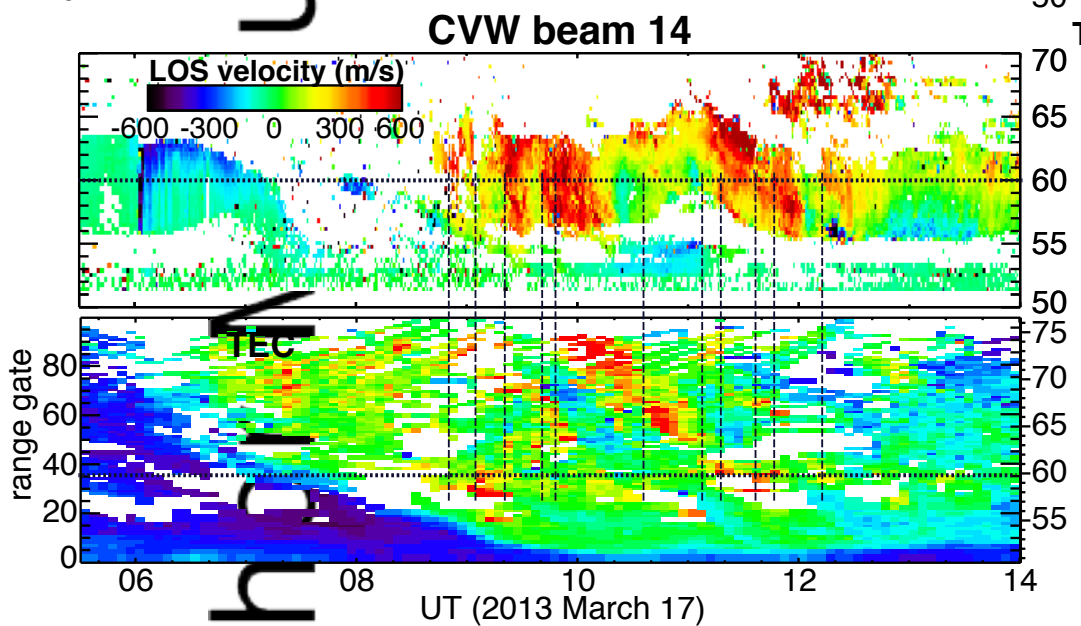
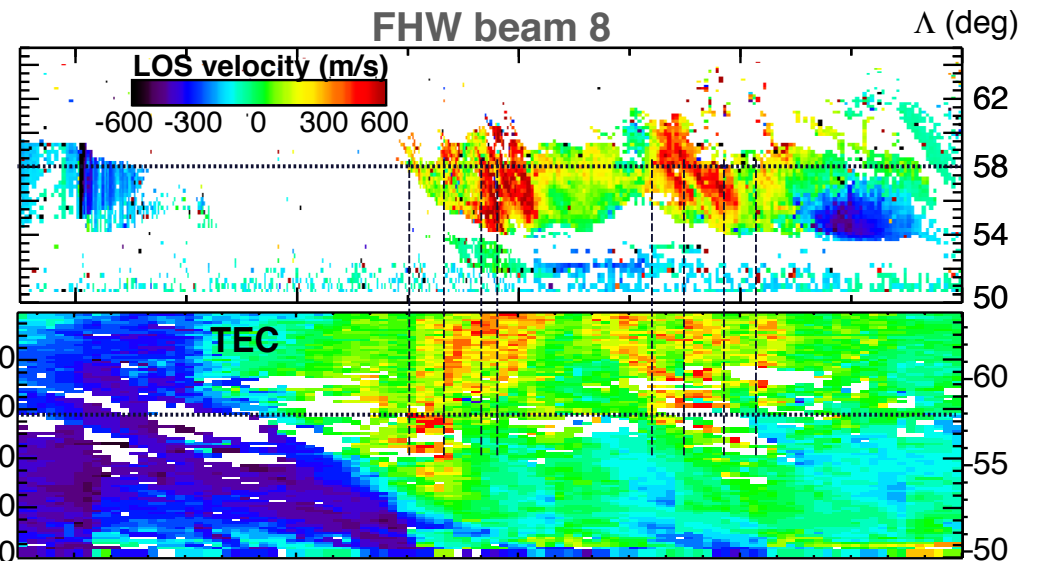
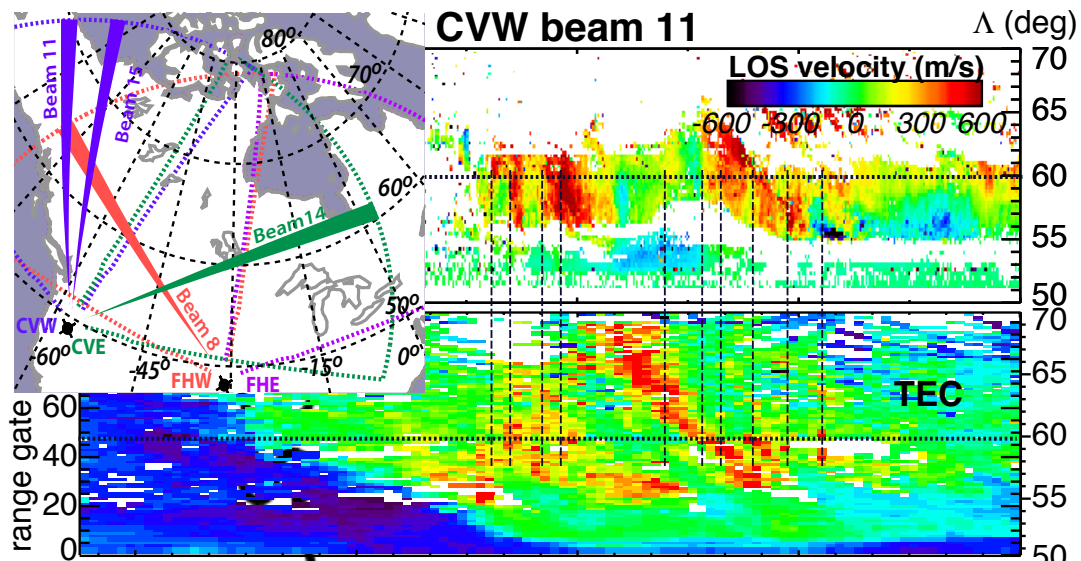


- DMSP oval poleward bndry
- DMSP oval equatw. elec bndry
- ┆ DMSP soft elec/proton bndry

AS

As this article is prepared, all rights reserved.





Auth

